

200. von Hippel AR (1956) Molecular engineering. *Science* 123(3191):315–317
201. von Neumann J (1956) Probabilistic Logics and the Synthesis of Reliable Organisms from Unreliable Components. In: *Automata Studies*. Princeton University Press, Princeton, pp 43–98
202. Waingold E, Taylor M, Srikrishna D, Sarkar V, Lee W, Lee V, Kim J, Frank M, Finch P, Barua R, Babb J, Amarasinghe S, Agarwal A (1997) Baring it all to software: Raw machines. *Computer* 30(9):86–93
203. Wang KL, Khitun A, Flood AH (2005) Interconnects for nanoelectronics. In: *Proc. 2005 IEEE International Interconnect Technology Conference, San Francisco, 6–8 June 2005*, pp 231–233
204. Wang W (1990) An asynchronous two-dimensional self-correcting cellular automaton. PhD thesis, Boston University, Boston, MA 02215, short version: In *Proc. 32nd IEEE Symposium on the Foundations of Computer Science, San Juan, 1–4 Oct 1990*. IEEE Press, pp 188–192, 1991
205. Weeber JC, González MU, Baudrion AL, Dereux A (2005) Surface plasmon routing along right angle bent metal strips. *Appl Phys Lett* 87(22):221101
206. Whitesides GM, Grzybowski B (2002) Self-assembly at all scales. *Science* 295(5564):2418–2421
207. Mac Williams FJ, Sloane NJA (1978) *The Theory of Error-Correcting Codes*. North-Holland, Amsterdam
208. Williams RS, Kuekes PJ (2001) Demultiplexer for a molecular wire crossbar network. US Patent 6 256 767
209. Winfree E, Liu F, Wenzler LA, Seeman NC (1998) Design and self-assembly of two-dimensional DNA crystals. *Nature* 394(6693):539–544
210. Wolf SA, Awschalom DD, Buhrman RA, Daughton JM, von Molnar S, Roukes ML, Chtchelkanova AY, Treger DM (2001) Spintronics: a spin-based electronics vision for the future. *Science* 294(5546):1488–1495
211. Wong HSP, Frank DJ, Solomon PM, Wann CHJ, Wesler JJ (1999) Nanoscale CMOS. *Proc IEEE* 87(4):537–570
212. Wood J, Edwards TC, Lipa S (Nov 2001) Rotary traveling-wave oscillator arrays: a new clock technology. *IEEE J Solid-State Circ* 36(11):1654–1665
213. Worschech L, Beuscher F, Forchel A (1999) Quantized conductance in up to 20 μm long shallow etched GaAs/AlGaAs quantum wires. *Appl Phys Lett* 75(4):578–580
214. Wu W, Jung GY, Olynick DL, Straznicki J, Li Z, Li X, Ohlberg DAA, Chen Y, Wang SY, Liddle JA, Tong WM, Williams RS (2005) One-kilobit cross-bar molecular memory circuits at 30-nm half-pitch fabricated by nanoimprint lithography. *Appl Phys A* 80(6):1173–1178
215. Yamada T, Akazawa M, Asai T, Amemiya Y (2001) Boltzmann machine neural network devices using single-electron tunneling. *Nanotechnology* 12(1):60–67
216. Yanagida T, Ueda M, Murata T, Esaki S, Ishii Y (2007) Brownian motion, fluctuation and life. *Biosystems* 88(3):228–242
217. Yang T, Kiehl R, Chua L (2001) Tunneling phase logic cellular nonlinear networks. *Int J Bifurc Chaos* 11(12):2895–2911
218. Zhirnov VV, Cavin RK, Hutchby JA, Bourianoff GI (2003) Limits to binary logic switch scaling – a gedanken model. *Proc IEEE* 91(11):1934–1939
219. Zhong Z, Wang D, Cui Y, Bockrath MW, Lieber CM (2003) Nanowire crossbar arrays as address decoders for integrated nanosystems. *Science* 302(5649):1377–1379

Nanoscale Atomic Clusters, Complexity of

ANATOLY I. FRENKEL¹, JUDITH C. YANG²,
DUANE D. JOHNSON³, RALPH G. NUZZO⁴

¹ Department of Physics, Yeshiva University,
New York, USA

² Department of Mechanical Engineering and Materials
Science, University of Pittsburgh, Pittsburgh, USA

³ Department of Materials Science and Engineering,
University of Illinois at Urbana-Champaign,
Urbana, USA

⁴ Department of Chemistry, University of Illinois
at Urbana-Champaign, Urbana, USA

Article Outline

Glossary

Definition of the Subject

Introduction

Synthesis of Nanoparticles Through Self-Assembly

Observation and Characterization:

Synergy of Experiments and First Principle Modeling

Structural Relaxation of Nanoparticles

Future Directions

Acknowledgments

Bibliography

Glossary

Nanoparticles These, also called nanoclusters, are atomic agglomerates having the size less than 100 nm at least in one dimension.

Bulk material The material which grain sizes are in the micrometer scale or larger.

Self-assembly method A method that a system uses to develop and form particular structure using only pre-existing components.

Definition of the Subject

Freestanding and supported, nanoscale metallic clusters (i.e., nanoclusters or nanoparticles) constitute complex systems as they span an enormous space of potential structures, each having different collective properties, with only few potentially stable (or metastable) structures that exhibit technologically beneficial properties. The synthesis and design of collective properties is a critical area of current research – with technological beneficial outcomes of ten equivalent to finding a “needle-in-the-haystack”. Yet

the synthesis and application of nanoparticles with specific properties has had, and will have, an increasing impact on technology, whether for improving toothpaste, 'green(er)' energy production (e.g., in petroleum refinement, catalysis, or batteries), biotechnology and national security issues (e.g., biosensors). From the perspective of theory, freestanding or supported nanoparticles constitute an enormous challenge in terms of property assessment as well as comparison of results, where the experimental processing routes to produce samples must be considered within theory for one-to-one comparison to measured data and understanding of the controlling physics to that observed.

Here we provide a glimpse into the complexity of the search space and a subset of the critical experimental and theoretical analysis tools that are capable of providing quantitative assessment of structure-property relations actually found, such as assessment of structure and reactivity, say, for catalytic performance. Hence, it is necessary (and desirable) to have a direct and meaningful coupling of experimental and theoretical analysis. It is our purpose to provide a brief overview of current quantitative methods and examples of such coupling of experiment and theoretical analysis.

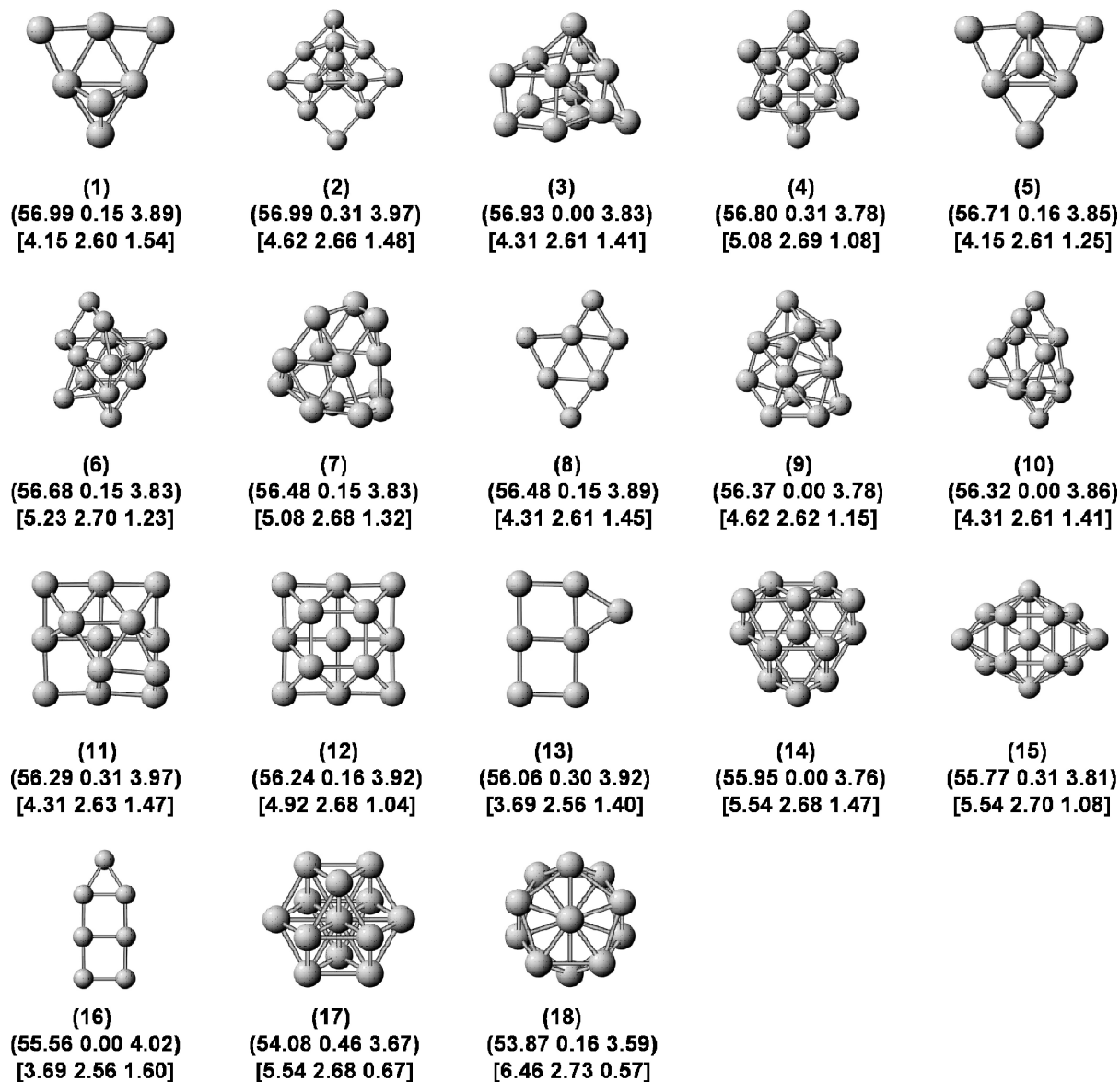
First, to exemplify the challenges, we provide an example list of issues. Even with an established synthesis route for a single-component nanoparticle, one cannot control with certainty the size, only the distribution – a narrow distribution is great but the nanoparticles properties will still depend, at a minimum, on surface-to-volume ratio (i.e., inversely as particle radii or size, $1/R$), an example of which is melting [1]. Already with a two-component nanoparticle, such as Pb-Bi, melting is controlled again in part by $1/R$ but also by thermal and electronically-driven effects such as chemical segregation, leading, for example, to shell-like nanoparticles with differing melting temperatures for inner and outer regions [2]. In addition, for a particle of fixed number of atoms, N , there can be an enormous number of structural isomers possible, or bonding motifs. For example, in Fig. 1 are the calculated lowest-energy, 13-atom ($N = 13$) freestanding isomers of Pt, [3] similar results have been obtained for other elements. From Refs. [3,4,5] it can be garnered (amongst many other points) that (i) high-symmetry structures are not necessarily low in energy, (ii) structures can be degenerate in energy, (iii) there is no simple correlation between structure and local properties, such as coordination number or bond lengths, (iv) both 3d and 2d structures compete in energy, and a structure (and concomitantly their properties) will be strongly affected by placing the particles on a support, and (v) intuition regarding

the important structures can be helpful but not reliable. Additionally, for fixed N and only two types of atoms (A and B) within the cluster $A_m B_n$, such that $N = m + n$, there are a binomial number $N!/(m!n!)$ of possible "alloy" configurations (i.e., homotopic groups of clusters, homomers that include stereoisomers) within a single structure (The term "homotops" has been introduced by J. Jellinek to describe such clusters that form homotopic groups. But, to be consistent with standard chemistry use of isomers and the general symmetry descriptions, such as enantiomers, diastereomers, and stereoisomers, we refer to these as homomers). There have been two recent and excellent reviews [6,7] thoroughly discussing these issues, mainly from a theoretical perspective. Finally, nanoparticles with structures that have useful properties may be only possible through self-assembly of organic stabilizers, e.g. Au nanoparticle stabilized via thiol ligands [8]. Clearly, the possible configuration space is daunting. Yet, it is critical that we can assess the structural properties of synthesized freestanding and supported nanoparticles in order to sort out many factors influencing their complex behaviors and correlate them with property design requirements. This is the principal scope of what follows, where we focus on the integrated use of several advanced analytic techniques – x-ray absorption fine structure (XAFS), and atom-counting methods of electron microscopy, and ab initio theoretical methods to achieve these goals and answer questions central for many complex systems, including nanoscale atomic clusters.

Introduction

Metallic nano-sized clusters (i.e., nanoclusters or nanoparticles) play a crucial role in modern science and technology. The application of design at the atomic scale can be found in petroleum refinement, catalytic converters, and nanofabrication. On a more academic level, metallic nanoparticle research can be found integrated in materials science, biotechnology, and organic chemistry [8]. Despite the ever-increasing interest of nanoparticles in different fields of study, catalysis remains perhaps the essential application of metallic nanoclusters, due to its potential technological impact.

The enhanced catalytic activity of these nanomaterials results from an increased number of atoms exposed to the surface compared to the corresponding bulk material. As a corollary, the number of neighbors to which a given atom is coordinated decreases, giving rise to nonbulk-like behaviors [9,10,11,12,13]. The energetic considerations of such systems lead to important synthetic pathways such as hydrogenation of olefins and silylation of polymers [14].



Nanoscale Atomic Clusters, Complexity of, Figure 1

Pt₁₃ isomers in order of decreasing binding energy calculated via density functional theory (see text). Properties listed below the structure are (in parentheses) energy (eV), magnetic moment (μ_B /atom), mean inter-atomic distance (Å), and [in brackets] first nearest-neighbor coordination number, first NN bond length (Å) and s-d hybridization index, see Ref. [3]. Structures 17 and 18 are the compact O_h and I_h isomers, and 14 is the 2-layer cuboctahedrally stacked cluster, which forms the basis of bulk fcc Pt. Reprinted figure with permission from [3]

The syntheses of these nanoscale materials can be categorized as physical or chemical methods. Physical methods involve a “top-down” approach where starting material is sculpted down to the atomic scale in the gaseous state. Once in the gaseous state the atoms can then condense into larger structures. Examples of physical methods in the synthesis of nanoclusters are metal-vapor depo-

sition [15,16,17] and laser ablation [15,18]. In both these methods different sources of energy are utilized to generate atoms from bulk material. Typically, the vaporized atoms are then deposited onto a substrate under vacuum, where particles form by nucleation [19]. Again, the reactive surface of these particles results in aggregation and reduction of the surface area leading to self-assem-

bly of a metallic cluster [20]. One of the drawbacks associated with this method of synthesis is the financial burden due to the expensive equipment required. Another limitation is the broad distribution of cluster sizes generated in the syntheses [15,18]. Yet despite recent advancements in physical methods for nanoclusters synthesis, [21,22,23] the field is predominantly controlled by chemistry [15].

Chemical methods take a “bottom-up” approach toward synthesis. Unlike physical methods, applying chemistry toward nanoparticle synthesis implies the assembly of the structures from chemical precursors. Traditionally, nanoparticle synthesis involves the reduction of metal salts in solution followed by the use of a capping agent to prevent aggregation of the particles. Reducing agents such as alcohols, [24] hydrogen gas, [25] and hydrides [26] can be used in the reduction of the ionic metal. Capping agents typically used are organic polymers, [24] as well as surfactants [25,26]. Coupling of the reducing and capping agent can be accomplished with molecules such as sodium citrate [27]. Chemical methods offer better control of particle size, with the assistance of capping agents, and greater flexibility because of the variety of chemical precursors that can be utilized in synthesis. In contrast to physical methods, fabrication of nanoparticles using chemistry is relatively inexpensive. Even with the improved precision intrinsic to chemical methods however, reproducibility of size, structure, and catalytic ability at the nanoscale regime (1–10 nm) is not concrete. On the other hand, developments in chemical synthesis of nanoparticles have opened doors toward other innovative methods of generating metallic nanoclusters [14].

Despite the relatively large number of available structural techniques, most of them obtain the overall, volume-average properties of nanoparticles, and give little, if any, insight into sometimes very elaborate *actual* arrangement of atoms within the particle. Two state of the art methodologies, synchrotron x-ray absorption fine-structure (XAFS) and quantitative scanning transmission electron microscopy (STEM) have been best positioned for determining the 3D structure and structural habits, both individually and as an ensemble, critical for understanding metallic nanoclusters. XAFS technique is one of the premiere tools to study both atomic and electronic structure of small ensembles due, in part, to its local structure sensitivity and excellent spatial resolution. By measuring coordination numbers, bond lengths and their disorder up to the 5th coordination shell, one can reliably determine the size of the nanoparticles, their shapes (e. g., oblate, raft-like, or truncated polyhedral), surface morphology as well as effects of surface disorder in 1–2 nm-size clusters as

a function of external conditions (temperature, alloy composition, support material, etc.).

Complementary information on site-specific structure and chemistry can be obtained by STEM, which has a unique capability for providing structural and spectral information simultaneously. Supported metal nanoclusters of size of 1–100 atoms make an ideal system for examination by high-angle annular dark-field (HAADF, also known as *Z*-contrast) imaging. Correlating the absolute image intensity to the scattering cross-section has been advanced recently within the STEM-based imaging method. With this improvement, one can directly count, with accuracy of ± 2 atoms, the number of atoms in a supported nanocluster avoiding complexities associated with coherent diffraction. By utilizing state of the art electron and x-ray probe methodologies, one can explore substrate/nanoparticle interactions as a function of support and nanoparticle material, as well as by size, composition and 3-D structure of the supported nanoparticles.

Most state-of-the-art experimental work is integrated with theoretical calculations to help interpret and accelerate identification of cluster bonding motifs, possible metastable structures, and determine electronic properties and reactivity of relevant clusters. Realistic nanometer-sized, metallic clusters (i. e., those equivalent to experiment) can be reliably simulated by electronic-structure and molecular-dynamic techniques to address the issues of complex geometries (cluster size and corresponding thermodynamically- or kinetically-stabilized shapes and atomic arrangement), of shape evolution (kinetics), as well as local bonding effects that determine reactivity. As such, a correlated, self-consistent interpretation of the experimental data from methods discussed above can accelerate identification of cluster bonding motifs, possible metastable and dynamic structures, and determination of the electronic properties of relevant clusters.

In the remainder of the article will first review the methods of synthesis of nanoparticles, including those guided by self-assembly (Sect. “Synthesis of Nanoparticles Through Self-Assembly”). The modern experimental and theoretical methods of nanoparticle analysis will be reviewed in Sect. “Observation and Characterization: Synergy of Experiments and First Principle Modeling”. Complexity of several typical cluster systems, mono- and bimetallic, supported and freestanding, will be illustrated by examples from recent works (Sect. “Observation and Characterization: Synergy of Experiments and First Principle Modeling”). Sect. “Structural Relaxation of Nanoparticles” discusses the possible origins of structural relaxation and surface reconstruction observed experimentally

and studied theoretically in ultra-small clusters. Future directions are outlined in the final section.

Synthesis of Nanoparticles Through Self-Assembly

Besides traditional methods of chemical synthesis, the field has expanded to include many other routes toward production of metallic nanoparticles. Among these newer techniques are photochemical synthesis, electrochemical synthesis and sonochemical synthesis. Another departure from standard chemical methods of nanoparticle synthesis is in the production of bimetallic nanoparticles [7]. The classic framework for creating nanoparticles, although efficient for some elements, requires various reagents and consequently rigorous reaction conditions [28].

Photochemically induced synthesis of nanoparticles offers the advantage of using ultraviolet light to assist in the reaction without the addition of capping or stabilizing agents [14,28,29]. The reduction reaction can be explained by the photoexcitation of a metal salt and organic molecules containing carbonyl groups. The photoexcitation of the organic compound often results in the formation of radical [28,30] or subsequent formation of a radical [29]. Reduction of the metal ion ensues by the formed organic radical. In the case of multivalent metals, reduction occurs until the atom reaches a neutral state and aggregation of a nanoparticle follows thereafter. Although the formed particles aggregate without the inclusion of a capping agent, crystal growth is mediated by the ionic liquid solution of the original reaction mixture. The surfaces are stabilized electrostatically by the concentration of ions in the solution [28,29]. Other methods of photochemical synthesis often use reducing agents which also serve as capping agents; physically adsorbing to nanoparticles and arresting further aggregation [30,31,32,33].

Another alternative to traditional methods of synthesis is sonochemistry. The inner workings of sonochemistry stem from the extreme temperatures and pressures achieved by the expansion and implosion of bubbles in solutions, a process known as cavitation [14,34,35]. The intense energy released upon collapse of the bubbles results in the decomposition of molecules and the formation of free radicals. As with photochemical synthesis, the resulting free radicals initiate the reduction reactions used to reduce the metal ions in solution [36]. Particle size is maintained by the use of capping agents [37,38,39]. The main advantages of using sonochemical methods are the fast reaction rates and the ability to generate very small sized nanoparticles. On the other hand, a broad distribution of particle sizes is also typically obtained from this type of synthesis [40].

Electrochemical synthesis of nanoparticles is another viable option capable of generating metallic nanoclusters. In this method an anode is placed in solution and oxidized in the presence of a chaperone molecules or stabilizing agents. The oxidized atoms from the anode migrate to the cathode where they are reduced. Aggregation shortly follows after the migration to the cathode where cluster growth is mediated by the stabilizing agents. Isolation of the particles is accomplished by precipitation of the product from the cathode [14,41,42,43]. There are methods where a rotating cathode [44] or a double pulse technique [45,46] is implemented to improve size distribution and yield, but ultimately the chemistry that occurs is identical to the standard electrochemical method. Comparatively, reduction using electrochemistry has many advantages over its counterparts. Once formed, the nanoparticles can be easily isolated as they begin to precipitate out of solution. The size of the clusters generated can be controlled varying the current intensity of the cell, [42,45,46] but perhaps the greatest advantage of this method is the high yields achieved [14].

Another area of synthesis important in the field of metallic nanoparticles is bimetallic nanocluster preparation. The interest in bimetallic nanoclusters arises from the changes in physical and chemical properties compared to monometallic species [47,48,49,50,51,52]. As with monometallic clusters, many routes exist toward the synthesis of bimetallic clusters. These materials can be synthesized by traditional forms of reduction, using metal ion-containing salts (precursors). Additionally, this system of reduction can be accomplished simultaneously or sequentially. In simultaneous synthesis both metallic precursors are reacted in the same solution in the presence of capping agents. The mixture can result in the spontaneous formation of a core/shell structure as well as other alloyed structures [39,53]. Alternatively, successive addition of the metallic precursors has proven to be a more efficient way to control particle structure [14,39,54,55]. In the successive method the formation of the initial metal cluster behaves as a nucleation site for the growth of the second metal, affording a core shell motif. Incidentally, this self-assembly of core/shell structures has been induced simply by the mixing of nanoclusters of two different metals [56,57]. The structural motif has been attributed to a balance between surface energies as well as binding energies where size and composition of the clusters is detrimental to structural refinement [56]. Studies have also shown that the core/shell structure can be inverted at extreme temperatures [53]. Furthermore bimetallic nanoclusters can be synthesized by using a sacrificial layer of hydrogen adsorbed onto the surface of the core metallic

cluster. Using the adsorbed hydrogen layer as a reducing agent, incoming metallic ions are reduced onto the surface of the core cluster forming a shell. Thus far this method has only been generated with specific metallic species [58]. In addition to the aforementioned methods of synthesizing bimetallic particles, synthesis can also be accomplished by sonochemical, [39] electrochemical [54] and photochemical [55] methods.

Observation and Characterization: Synergy of Experiments and First Principle Modeling

Combination of complementary structural techniques – electron microscopy and XAFS, as well as DFT/MD simulations, provide previously unavailable atomic-level understandings of the structural dynamics of the most important forms of supported metal clusters. These methods can provide understandings of the metal framework bonding present in supported nanoscale clusters and the significant impacts on them that can originate as a consequence of adsorbate bonding and (more recently revealed) electronic effects mediated by support interactions. The data from microscopy now allows one to establish precise atomic compositions in supported catalyst systems, counting atoms explicitly at the single nanoparticle level. Experimental protocols based on synchrotron x-ray absorption spectroscopy allow the elucidation of the precise structural habits adopted by supported forms of metallic nanoparticles – establishing methodologies of modeling that define the nature of the strains present in such systems; unraveling the complex nature of the atomic level bonding habits they embed; the dynamical factors that mediate transformations of these structures due to the impacts of particle size, temperature-dependent support interactions, and adsorbates; the nature of the size-dependent atomic-bond relaxations that these particles embed; and the nature of the complex electronic structures that are unique to materials of this sort [59,60,61,62,63,64].

Development and testing of these advanced methods rely on the availability of synthetic methods that have provided model systems – both in the form of discrete monolayer protected clusters and supported metal nanoparticle catalysts – with precisely defined compositions and (for the latter) extremely narrow distributions of atomic mass.

Metal nanoclusters [65] (and gold nanoclusters in particular [66]) can exhibit structures that differ significantly from that corresponding to the bulk, ones that depend strongly on cluster size. Detailed knowledge of these structures is crucial for understanding and predicting nanocluster properties, including chemical, electrical, magnetic, and optical ones. The experimental determination

of atomistic structural information is a very difficult task: analyses by imaging or scattering methods are presently limited by insufficient spatial resolution or by the coherent scattering size of these techniques. As a result, most structural determinations proceed indirectly by comparing experimentally accessible properties (e. g., ion mobility, photoemission spectra, polarizability, optical absorption, etc.) with those computed theoretically for candidate structures. Synergistic approaches, however, combining several structural techniques into a self-consistent structure refinement method, make accessible the previously unknown physical picture of the nanoscale. In the following sections, we will show examples of the determination of size, shape and atomic structures of mono- and bimetallic nanoparticles by combining results of extended x-ray absorption fine-structure (EXAFS), advanced methods of electron microscopy and DFT/MD calculations.

Structure Determination by EXAFS

By using EXAFS technique, one can extract accurate information about the identities, average distances, and coordinations of the neighboring atoms to the x-ray absorbing atom in nanoclusters [67,68]. The EXAFS signal, $\chi(k)$, is the sum of all contributions, $\chi_i(k)$, from groups of neighbors at approximately equal distances from the absorbing atoms (i. e., the i th shell), which are often written as: [69]

$$\chi_i(k) = \frac{S_0^2 n_i}{k R_i^2} \left| f_i^{\text{eff}}(k) \right| \cdot \sin \left[2kR_i - \frac{4}{3} \sigma_i^{(3)} k^3 + \delta_i(k) \right] e^{-2\sigma_i^2 k^2} e^{-2R_i/\lambda_i(k)}, \quad (1)$$

where k is the photoelectron wave number, $f_i^{\text{eff}}(k)$ and $\delta_i(k)$ are the photoelectron scattering-path amplitude and phase, respectively, S_0^2 is the passive electron reduction factor, n_i is the degeneracy of the scattering path, R_i is the effective half-path-length (which is equal to the interatomic distance for single-scattering paths), σ_i^2 is the mean-square deviation in R_i , $\sigma_i^{(3)}$ is the third cumulant, and $\lambda_i(k)$ is the photoelectron mean free path. Using modern computer packages, e. g., IFEFFIT, [70] which employs a non-linear least square method to fit theoretically calculated (with the help of FEFF6 code [69]) EXAFS signal to the data, one can obtain the best-fit values of structural parameters, together with their uncertainties. The mean-square deviation, σ^2 , of the first nearest neighbor (1NN) distance can be represented to a good approximation as a superposition of static (σ_s^2) and dynamic (σ_d^2) terms:

$$\sigma^2 = \langle (r - \langle r \rangle)^2 \rangle = \sigma_s^2 + \sigma_d^2. \quad (2)$$

To separate the temperature-independent σ_s^2 and temperature-dependent σ_d^2 , one can use a simple correlated Einstein model for σ_d^2 :

$$\sigma_d^2 = \frac{\hbar}{2\omega\mu} \frac{1 + \exp(-\Theta_E/T)}{1 - \exp(-\Theta_E/T)}, \quad (3)$$

where ω is a bond vibration frequency, μ is the reduced mass of the 1NN atomic pair, and $\Theta_E = \hbar\omega/k_B$ is the Einstein temperature. Thus, the total σ^2 in this approximation depends on three parameters: T , Θ_E , and σ_s^2 . By replacing the total σ^2 in Eq. (2) by a sum of the dynamic and static terms (Eq. (2)), the best fit results for Θ_E and σ_s^2 can be obtained from a concurrent non-linear least square fitting of Eq. (2) to the EXAFS data taken at various temperatures. From obtaining the best fit values, with their uncertainties, of n_i , R_i , σ_s^2 , σ_d^2 and $\sigma_i^{(3)}$, one can significantly reduce the number of possible models of cluster structure and its interaction with the environment (thermal effects, gas atmosphere effects, cluster-substrate, cluster-adsorbate interactions, etc.) EXAFS, however, only yields ensemble-averaged information; thus its application is most valuable for structure refinement of size-controlled nanoclusters.

There are several approaches that allow one to estimate cluster size from EXAFS results. The most popular method is using the first nearest neighbor (1NN) coordination number n_1 that can be directly obtained in EXAFS analysis. These data can be compared against *exact* cluster models or approximate expressions. For the first approach, calculations of Montejano-Carrizales et al. [71] are useful as they obtained geometrical characteristic of several regular polyhedral clusters (cubo-octahedral, icosahedral, body-centered cubic and simple cubic) analytically as a function of the cluster order L . Defining $L = N_E - 1$, where N_E is the number of atoms along the edge of a regular polyhedron, the following relationships can be derived for the 1NN coordination numbers in cuboctahedral (closed packed) and icosahedral (non-closed packed) clusters that have the same sequence of their magic numbers ($N = 13, 55, 147, 309, 561, 923 \dots$): [71]

$$\begin{aligned} n_1^{\text{co}} &= \frac{24L(5L^2 + 3L + 1)}{10L^3 + 15L^2 + 11L + 3}, \\ n_1^{\text{icos}} &= \frac{6L(20L^2 + 15L + 7)}{10L^3 + 15L^2 + 11L + 3}. \end{aligned} \quad (4)$$

Calvin et al. [72] used the second approach by approximating the cluster shape as a sphere with radius R and obtaining the 1NN coordination number for a cluster with average 1NN distance r as follows:

$$n_1 \approx \left[1 - \frac{3}{4} \left(\frac{r}{R} \right) + \frac{1}{16} \left(\frac{r}{R} \right)^3 \right] n_1^{\text{bulk}}.$$

This approach is advantageous for larger clusters, and when the size distribution is relatively broad.

The method of measuring of 1NN coordination numbers for size determination in supported metal particles dates back to the end of 1970s [73,74,75,76,77,78,79, 80,81,82,83,84]. An early publication detailing an analysis of the structures of supported Pt nanoparticles by EXAFS, found a strong correlation between the measured first nearest neighbor (1NN) metal coordination number and the disorder of their bond lengths; lower coordination numbers appeared to correlate strongly with increased measured disorder in the first-shell metal-metal bond lengths [73]. These effects would be most sensitively seen in particles of the smallest size. The importance of anharmonic corrections to the 1NN pair interaction potential had yet to be appreciated in this pioneering work. Neglecting this effect leads to a non-physical decrease in 1NN bond lengths measured at high temperatures. Enhanced disorder in the 1NN bond distance was later correlated with the influences that result from cluster-support interactions [79]. These studies provide an important insight into the nature of supported metal nanoparticles, namely that the bond lengths of surface atoms should exhibit enhanced structural disorder.

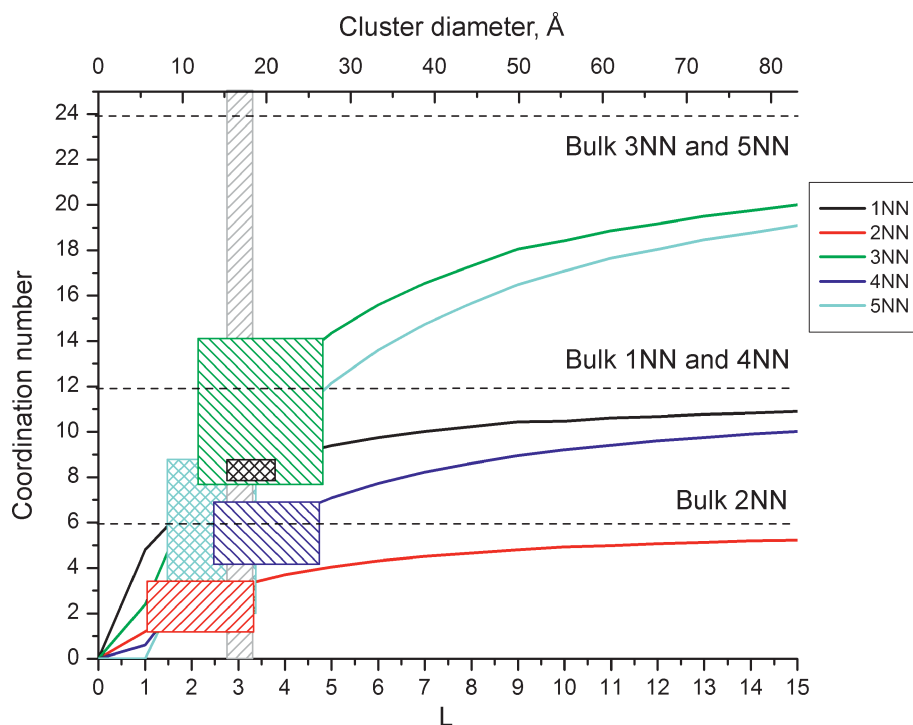
Another approach, to use size-dependent 1NN distance change as a measure of cluster size, was used by Frenkel et al. [61] to obtain sizes of alkanethiolate-stabilized Au nanoparticles. Such changes were first observed by Mays et al. [85] and attributed to surface tension (ST) in the framework of liquid drop model of nanoclusters. To analytically estimate particle diameter, d , the ST method utilized the equation:

$$d = \frac{4}{3} f_{\text{rr}} K \alpha,$$

where f_{rr} and K are the surface stress and compressibility in the bulk, and $\alpha = \Delta R/R$ is the relative lattice contraction that can be measured by EXAFS. Montano et al. [86, 87,88] studied Fe, Cr, Ag and Cu nanoclusters by EXAFS and observed contractions of the average interatomic distances relative to the bulk in all cases.

An alternative approach by Jiang et al. [89] is based on the surface multiplayer relaxation phenomenon, proposed by Finnis and Heine [90]. According to their model, cluster interatomic distances can be calculated for an arbitrary polyhedral shape, using known experimental relaxation data for macroscopic crystal surfaces.

The 1st shell methods described above are based on analytical calculations of the coordination numbers or distances as a function of particle size. However, when clusters are asymmetric, these methods are not accurate since



Nanoscale Atomic Clusters, Complexity of, Figure 2

Cluster size, shape and structure determination: comparison of the average coordination numbers (up to 5NN), together with their error bars, measured by EXAFS for the carbon-supported Pt nanoparticle sample and those predicted from the truncated cuboctahedron model for various cluster sizes. Reprinted with permission from [68]

model values of n_1 may be similar when not only the size, but the shape and structure of the cluster are allowed to vary. Only when coordination numbers (or path degeneracies) corresponding to the more distant shells and multiple-scattering contributions are measured, one will have a series of indices: $\{n_i\}$, $i = 1, 2, 3 \dots$ which should be unique for any given polyhedral cluster model. Since multiple-scattering contribution to EXAFS in nanoclusters can be quantitatively analyzed, [91] not only the single-scattering coordination numbers but also multiple-scattering path degeneracies could be reliably extracted from the EXAFS data. Such additional information effectively communicates size, shape and surface orientation of nanoclusters (Fig. 2) [68].

Even though the methods above can be used to describe metal-metal coordination numbers and, therefore, size, shape and structure information in monometallic and heterometallic clusters, the latter are characterized by significantly higher level of complexity, due to their chemical heterogeneity.

In bimetallic clusters, two distinctly different types of mixing of A and B atoms are possible. They can be mixed statistically (i. e., randomly, in accordance with the

overall concentration) or non-statistically. The most common example of non-statistical mixing is segregation of atoms of different elements, forming a core-shell-type particle where larger than the concentration-weighted average number of atoms of one type can be found in the core, and the other type – at the surface of the particle. In heterogeneous samples, where different clusters (A-rich and B-rich) can be formed, the situation may be further complicated [92].

For *random* alloys, the average coordination numbers n_{AA} and n_{AB} of A and B atoms relative to A atom are in the same proportion as the bulk concentrations of these elements in the sample:

$$\frac{n_{AA}}{n_{AB}} = \frac{x_A}{x_B}.$$

For alloys with nonzero short range order, the left part may be *larger* or *smaller* than the right part, indicating *positive* or *negative* tendency to clustering, respectively. In the former case, the atoms A and B segregate to different regions of the nanoalloy. In the latter, the A atoms are preferentially coordinated with B (with probability greater than x_A/x_B) and vice versa.

We can also introduce a short range order parameter, α , analogously to its definition by Cowley for bulk alloys: [93]

$$\alpha = 1 - \frac{n_{AB}/n_{AM}}{x_B},$$

where $n_{AM} = n_{AA} + n_{AB}$ is the coordination number of the A-metal bonds. For alloys with positive or negative tendency to clustering, α will be positive or negative, respectively. However, even after the segregation is demonstrated by examining the experimental values of n_{AA}/n_{AB} or α , more experimental information is still needed to find out whether A is predominantly in the surface or in the core, as well as for the determination of the particle size.

Such information is available by measuring EXAFS on both A and B central atoms and extracting coordination numbers n_{AA} , n_{AB} and n_{BB} . The analysis should be done concurrently, with obvious constraints imposed on the heterometallic bonds during the fits: [94]

$$n_{AB} = \frac{x_B}{x_A} n_{BA}; \quad R_{AB} = R_{BA}; \quad \sigma_{AB}^2 = \sigma_{BA}^2$$

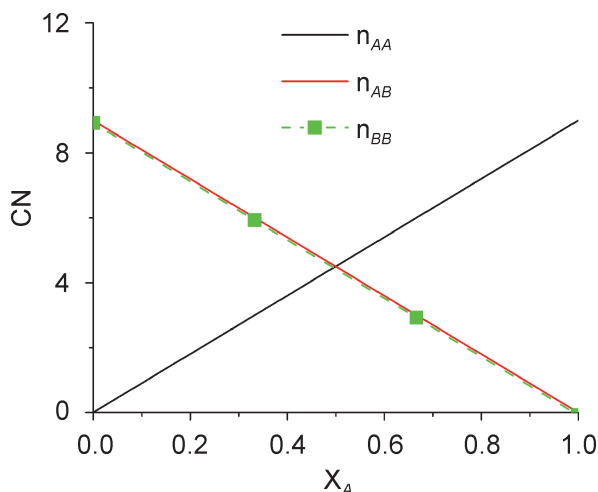
The atoms of the type A will segregate to the surface of the nanoparticle and B – to the core, if $n_{AM} < n_{BM}$, since atoms at the surface have fewer neighbors than those in the core. This criterion is useful even for alloys containing elements that are neighbors in periodic table (e. g., Fe-Ni, Pd-Ag, etc.) where only the total n_{AM} , n_{BM} numbers can be measured by EXAFS analysis of A and B absorbing atoms, respectively, due to the similarity of backscattering amplitudes of A-A and A-B pairs (as well as B-A and B-B). Another advantage of analyzing both A and B EXAFS data is for the particle geometry determination. Indeed, the average number of metal-metal neighbors per metal atom:

$$n_{MM} = x_A n_{AM} + x_B n_{BM}$$

for the first nearest neighbor shell, combined with other information (e. g., higher shell coordination numbers, transmission electron microscopy (TEM) data, etc.) allows one to estimate the particle size by methods similar to those described above for monometallic particles.

Random bimetallic alloys have a unique behavior of these coordination numbers with concentration. Assume, for simplicity, a bimetallic nanoparticle of a certain size, with random distribution of A and B atoms, where the following relationships apply:

$$\begin{aligned} n_{AM} &= n_{BM} = n_{MM}; & n_{AA} &= n_{BA} = x_A n_{MM}; \\ n_{BB} &= n_{AB} = x_B n_{MM} & &= (1 - x_A) n_{MM}. \end{aligned}$$



Nanoscale Atomic Clusters, Complexity of, Figure 3
Theoretical partial coordination numbers in random nanoalloys (assuming $n_{MM} = 9$) as a function of composition

Thus, partial coordination numbers should depend *linearly* on alloy concentration (Fig. 3) in *random* nanoalloys, provided that the particle size is the same at all concentrations.

Structure Determination by Advanced Methods of Transmission Electron Microscopy

As mentioned above, while multiple-scattering (MS) EXAFS allows determination of the bonding geometry in the nanoscale, it does so in the form of ensemble-average information. Advanced TEM and scanning TEM (STEM) methods, on the other hand, can probe the atomic-level structure and chemistry of individual nanoparticles and allow direct visualization of nano-scale phenomena [59]. Modern electron microscopy is a powerful tool which, if used in conjunction with EXAFS, can provide a wealth of information about the samples which otherwise could not be determined if these techniques were not used synergistically.

Using “Z-contrast” protocol in STEM, one can correlate the absolute image intensity to the scattering cross-section, so that the number of atoms can be counted experimentally. Furthermore, high-resolution electron microscopy (HREM) can visualize the facets and shapes of nanoparticles and the interfacial structures between the nanoparticles and their supports. In this way, a full mapping can be made of the structural landscape present in a complex heterogeneous sample.

Transmission electron microscopy has been used extensively and successfully to study nanoparticles [95]. It

has a higher level of accuracy than other methods for samples containing small number (< 100) of atoms [59]. Specifically, TEM methods have been used to examine clustering sites as well as the shapes of various clusters [95]. For example, one specific problem of interest in current heterogeneous catalysis research is determining the elemental distribution in a bimetallic catalyst particle, e. g., homogeneous distribution of elements or core-shell structures with separation of elements to the core and surface of the particles. In addressing these questions, TEM yields a wealth of information. Conventional TEM is capable of direct visualization at the resolution level of < 0.3 nm in standard instruments and < 0.1 nm in aberration-corrected microscopes. Such resolution allows the investigation of structure of catalysts at atomic level. Transmission electron microscopy uses a parallel beam of electrons, whereas analytical TEM, or STEM, methods employ a scanning attachment on the instrument that focuses the electron probe to enable energy dispersive spectroscopy (EDS) and electron energy-loss spectroscopy (EELS) detection to study elemental distribution as well as oxidation states from specific nanostructures in the sample. For example, a VG-STEM is an ultrahigh vacuum (UHV) instrument, and very fine probe (~ 0.5 nm diameter) with the ability to simultaneously image (Z-contrast) and collect EDS and EELS to acquire both structure and elemental distribution information.

One of the most common TEM techniques is HREM, which is based on phase contrast, and has been used extensively in nanoparticle studies as well. Thomas and Midgley [96] note that the two major techniques in utilizing HREM for atomic and nano-scale structures are the multislice method and basic electron diffraction studies which are analogous to x-ray crystallography. In using the multislice method one essentially matches theoretical quantum mechanical calculations of the electron diffraction patterns of the sample with the closest data set taken in order to infer information on the electronic and crystal structure of the sample [96].

The method works by essentially dividing the reciprocal space into “slices” with an “electron field/wave function” corresponding to each slice. The n th field of the n th slice is given by [97]:

$$\phi_{n+1}(b - \Delta b) = [\phi_n(b) \cdot q_n(b)] * \left(\frac{k_z}{z}\right) p(b)$$

where b is a reciprocal space vector and Δb is the shift in the origin of the wave function and the surface at each slice. $q_n(b)$ is the “phase grating” and $p(b)$ is the free space propagator. The asterisk represents the convolution of the two functions [97].

Transmission electron microscopy has an additional advantage over other techniques such as atomic force microscopy (AFM) in that the analysis of x-rays created by the electron beam/sample interaction can be used for elemental mapping [96]. The physical and chemical structure of the sample, e. g., bond structure (or electronic structure) can be obtained via analysis of the EELS. From the energy spectra of scattered or transmitted electrons, one can determine specific processes that occur in the sample, i. e., plasmon resonances and phonon excitations. These in turn offer a way to determine the electronic structures which give rise to such events in the material. The techniques include energy loss near edge structure (ELNES) which contains the chemical bond information. One can also coordinate the various states of excited atoms using the extended energy loss fine structure (EXELFS), a technique similar to EXAFS.

Determining the density of states and electronic structures of material interfaces is of particular importance in catalysis because the electronic structure at the interface governs aspects of adsorption, charge transfer and bonding. Thus EELS can be viewed as complementary to the other techniques mentioned above in allowing a detailed understanding of the chemical properties of individual nanoparticles [95] as well as their interaction with the substrate surface [98]. For example, Liu found that by using EELS analysis on a Pd-Ni bi-metallic system he could determine structural information about the thickness of Pd shell layer [98].

Perhaps the most important set of tools in nanocatalysis studies are incoherent elastic scattering techniques that are usually performed at large scattering angle. In the case of the high-angle scattering signals the incoherent scattering intensity of the signals depends on the atomic number, Z , as described by Rutherford scattering theory, which is ideal for imaging heterogeneous catalytic materials where high Z metals, e. g., Pt, are dispersed on a low Z support, e. g., alumina. Quantitative STEM which is based on high-angle annular dark-field (HAADF), or quantitative Z-contrast imaging, is the technique based on the acquisition of these very high scattering signals (> 96 mrad) [95]. HAADF is especially powerful in catalysis studies because the electronic structure and catalytic activity are directly related to the number of atoms in the particle [95]. Because many particles can be imaged simultaneously by HAADF, then this quantitative STEM method provides better statistical information, such as particle size distributions [95]. A major advantage of STEM over HREM is that the technique readily allows for EELS analysis, and x-ray emission analysis at the nano-level where scattered electrons can be simultaneously collected [96,99].

Z-contrast exploits nonlinear interference effects between the wave-packets of the scattered electrons [99]. The intensity of scattered electrons can be obtained from the expression for Rutherford scattering cross section:

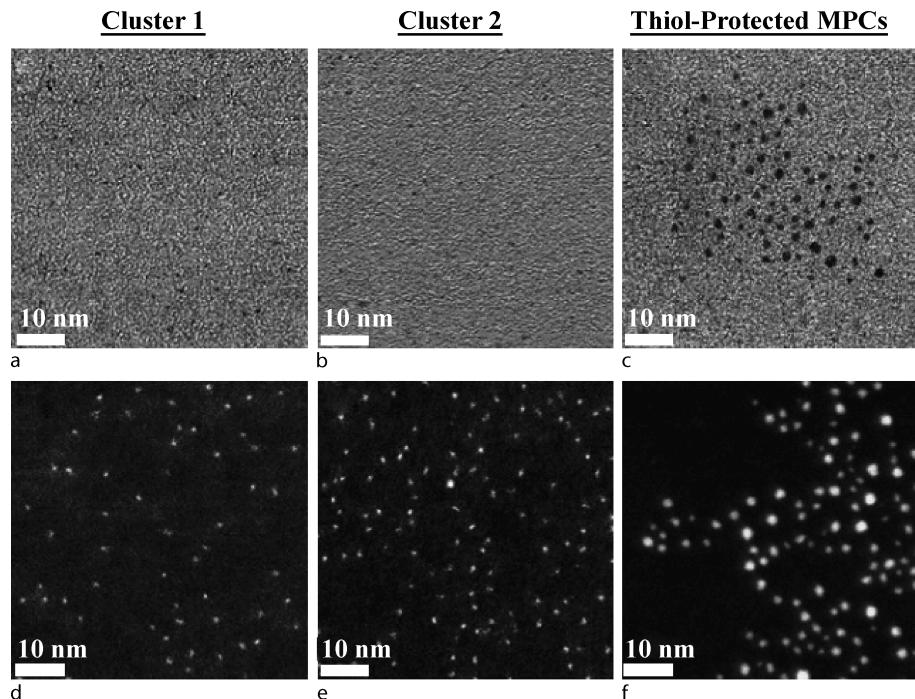
$$\frac{d\sigma}{d\Omega} = \frac{1}{16} \left(\frac{Z^2 e^2}{p^2/2m} \right) \left(\frac{1}{\sin^4(\theta/2)} \right)$$

Since the differential cross-section of the scattered electrons is proportional to Z^2 . A large contrast exists between the supporting structures and the nanoclusters in the image. By collecting electrons scattered to very high angles (> 96 mrad), one can suppress the in-column coherent such that the intensity of the image is simply the number of atoms in the cluster times the intensity expected for one atom of that element. Individual atoms in a particle within the sample may be counted provided that the detector has been properly calibrated. When the calibration is done, one then simply divides the total measured cross section by the cross section of an individual atom [100].

As can be seen in the Fig. 4, the contrast between the standard bright-field (BF) STEM images and the Z-contrast images can be striking. The images are those of monolayer protected gold nanoparticles. There is a large

contrast in the HAADF image where one can distinguish between two elements of greatly varying atomic numbers, namely the higher atomic number gold versus carbon [101]. In that particular study Z contrast was successfully employed to determine particle diameters of the various gold clusters as well as count atoms in individual particles [101].

Since the scattered signal is directly proportional to the number of atoms in the scattering center, one can calculate particle diameters measuring both the intensity profiles of the gold and then subtracting the profile of the substrate/supporting material alone, resulting in that of the gold particles [101]. Intensity profiles across the individual gold particles can then be plotted and measured at full width at half maximum (FWHM). The relationship between the number of atoms in the particle and its diameter is characteristic of the particle's shape. By comparing the relative intensities as a function of particle size, one can infer the nucleation and growth behavior of the particles. In general, the measured intensity and particle growth modes are intimately related [101]. If the intensity is directly proportional to the diameter cubed then it can be inferred that the particles are growing uniformly in three dimensions. However, if the intensity is proportional to the diameter



Nanoscale Atomic Clusters, Complexity of, Figure 4

Representative BF-STEM images of **a** mixed ligand (thiols/phosphines) Cluster 1, **b** mixed-ligand Cluster 2, and **c** thiol-protected clusters. Representative HAADF-STEM images of **d** Cluster 1, **e** Cluster 2, and **f** thiol-protected clusters. All images collected at 1 Mx magnification. Parts **a** and **d** are images of the same area collected simultaneously. Reprinted with permission from [100]

squared, the particles are seen to be forming a two-dimensional mono-layer or bi-layer [102].

The annular dark-field detector is calibrated by tilting the beam directly onto the HAADF detector, such as by using micro-diffraction mode, with an attenuated electron beam current in order to prevent saturation of the detector. In calibrating the dark-field (DF) detector the current is reduced by a factor of 100. The image of the HAADF detector provides the angular dependence of the detector efficiency, which is taken into account when quantifying the experimental electron scattering [100]. The nanoparticles are then imaged using the very high angle annular dark-field detector such that electrons scattered above ~ 100 mrad contribute to the image intensity. The number of atoms can be quantified as follows:

$$N_0^{\text{high}} = \left(\frac{\sum_{\theta=\beta_{\text{min}}}^{\theta=\beta_{\text{max}}} N_0^{\text{low}}(\theta) f(\theta)^2 2\pi \sin \theta d\theta}{\sum_{\theta=\beta_{\text{min}}}^{\theta=\beta_{\text{max}}} f(\theta)^2 2\pi \sin \theta d\theta} \right) \left(\frac{I_{\text{high}}}{I_{\text{low}}} \right)$$

where β_{min} is the inner detector angle (130 mrad), β_{max} is the outer detector angle, N_0^{low} is the detector response at the attenuated current, $f(\theta)$ is the atomic electron scattering factor of the element, I_{high} is the current of the electron beam used to image the particles, and I_{low} is the attenuated beam current used to image the detector for calibration [100]. Once the calibrations have been performed the intensity of scattered electrons from the nanoparticles can be measured and the background signals can be subtracted. Once the particle intensities are determined the data can be used to count the number of atoms.

Menard et al. demonstrated the utility of these techniques in studying gold nanoparticle monolayer protected clusters on carbon supports using the quantitative HAADF method and EXAFS [59,100,102]. By utilizing these techniques in tandem, characterization of the ligand-protected Au₁₃ nanoparticle size, shape, and structural disorder was accomplished. with an uncertainty of about three atoms. The combination of techniques allows for a detailed analysis of the transitioning point in terms of numbers of atoms, between classical and quantum behaviors or “bulk metallic and molecular states” as well as supporting the theoretical calculations such as those of the scattering amplitudes [59]. In these studies the HAADF imaging was performed with a field-emission Vacuum Generator HB501 STEM at 100 kV. The “atom counting” images were taken at 1-million magnification and have dimensions of 1024 × 1024 pixels.

Further HREM measurements were performed utilizing a field-emission JEM 2010F TEM/STEM operated at 200 kV to confirm the size and observe the crystallinity of the individual nanoparticles [59]. The importance of us-

ing the quantitative Z-contrast and HREM data is that it provides a set of constraints on the interpretation of corresponding EXAFS data as well as determines the grafting density of thiolates on the surface of the particles [59].

This summary demonstrates that high spatial resolution electron microscopies (such as quantitative Z-contrast) and HREM, are extremely useful in determining the behavior of nanomaterials, including nanoparticles, whose properties are transitional between “bulk” and “molecular” materials.

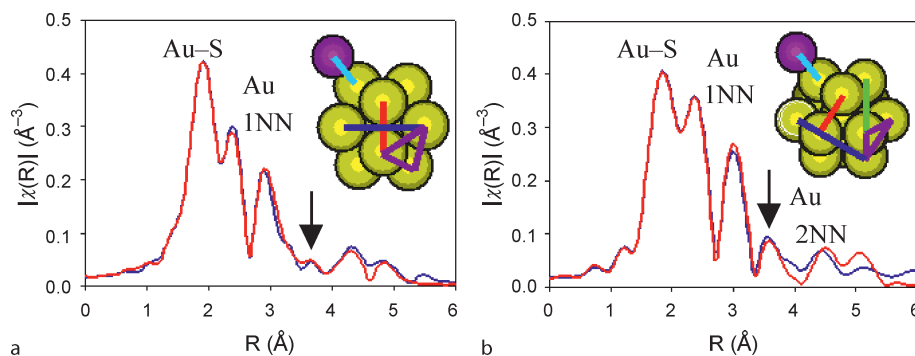
Cluster Studies by First Principle Theories and Molecular Dynamic Simulations

Theoretical methods also can greatly advance understandings of catalytic materials. First-principles, molecular dynamic (MD) simulations based on density functional theory (DFT) have been advanced to a point now where they can play a significant role in the interpretation of experimental data, revealing critical factors that determine and underlie specific metal cluster properties, see recent reviews [6,7]. (For brevity no attempt is made to include the many pertinent theoretical investigations and new methods, only a few critical papers regarding each key issues.) It immediately becomes more difficult to do this, however, as the cluster size or the chemical complexity (such as due to promoters, defects, adsorbates) of the system is increased, as noted already. In such cases, the DFT search space becomes daunting. Theory then becomes increasingly dependent on the direct experimental input and the availability of computing resources. Even with such capacities, however, the ability to identify relevant low-energy structures lying within a complex, and chemically rich, energy landscape remains a significant challenge and the insights coming from chemical “intuition” remain an important resource for developing useful analytical models.

Examples of Integrated Methods of Cluster Analysis

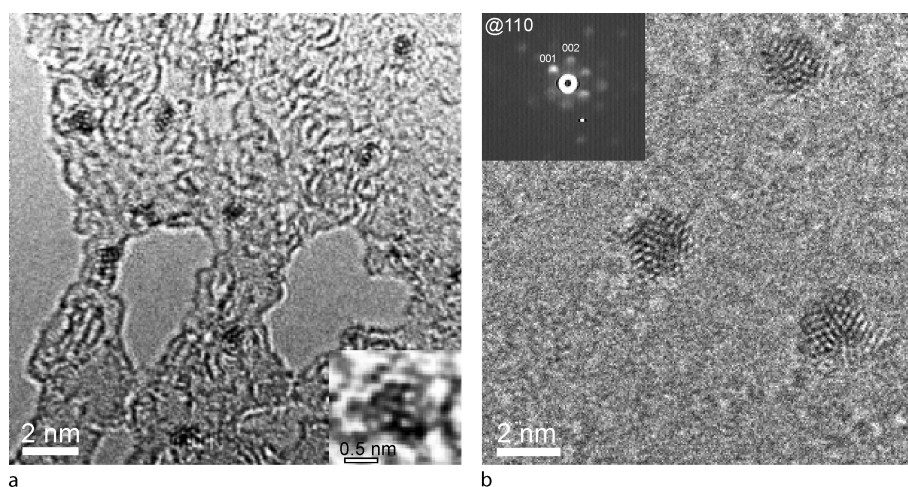
A recent combination of EXAFS and atom counting methods of transmission electron microscopy (TEM) on such specially-synthesized nanoclusters (Au₁₃[PPh₃]₄[S(CH₂)₁₁CH₃]₄) has found them to be highly monodisperse, with their overall structure possessing, on average, 13 gold atoms, with Au-Au coordination number of 6.7 ± 0.7 , an average Au-Au bond length of 2.85 ± 0.02 Å, and an average Au-ligand distance of 2.324 ± 0.007 Å [59]. The presence of eight ligands per cluster was deduced from x-ray photoelectron spectroscopy data [100].

The data presented in Fig. 5a,b illustrate such integrated analyses as applied to several Au nanoclusters – the



Nanoscale Atomic Clusters, Complexity of, Figure 5

Fourier transformed EXAFS spectra (blue) and fits (red) for **a** $\text{Au}_{13}(\text{PPh}_3)_4(\text{SC}_{12})_4$, and **b** fully-thiolated clusters. The insets show icosahedral (**a**) and truncated octahedral (**b**) units. The arrow indicates the fingerprint of the 2NN path in the closed packed structure (shown green in the inset) missing in the icosahedral clusters (**a**) but present in the truncated octahedral ones (**b**)



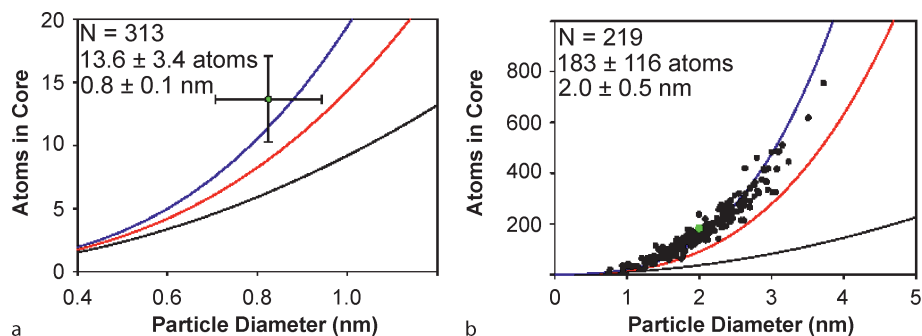
Nanoscale Atomic Clusters, Complexity of, Figure 6

a High-resolution electron micrograph of the mixed-ligand clusters. The inset shows a filtered image of a single cluster with icosahedral structure. **b** Thiol-protected MPCs with cubic packing. The inset shows an indexed μ -diffraction image taken from a single particle with a 2 nm diameter. Reprinted with permission from [59]

new mixed-ligand $\text{Au}_{13}[\text{PPh}_3]_4[\text{SC}_{12}]_4$ as well as a monolayer-protected cluster (MPC) system comprised of larger thiol-protected particles. The differences seen in the EXAFS data (Fig. 5) are profound and can be directly related to features of the atomic-level bonding present in each case. The mixed-ligand clusters adopt quasi-spherical shapes for their 13 atom cores (Figs. 6, 7). The full analyses unambiguously establish that an icosahedral geometry is present in each case, a bonding motif that stands in marked contrast with the *fcc* truncated octahedral structures adopted by the larger, fully thiolated MPCs (Fig. 5). These interpretations were independently verified by HRTEM and electron microdiffraction measurements (Fig. 6), and Z-contrast technique (Fig. 7) which identi-

fied the same structural motifs, albeit with less accurate detail [59,100].

While the combination of the experimental results points towards an icosahedral shape of the Au_{13} core, theoretical verification and a detailed interpretation of such a model was lacking. In particular, two central questions – ligand placement and anomalously high Au-Au bond length disorder – were left unanswered by the experimental results. First, EXAFS is not capable of discriminating between Au-S and Au-P neighbors, treating them cumulatively as Au-L ($L = \text{S/P}$) pairs and obtaining the overall Au-L coordination number as the total number of Au-S and Au-P bonds divided by the total number of Au atoms. However, the phosphines and the thio-



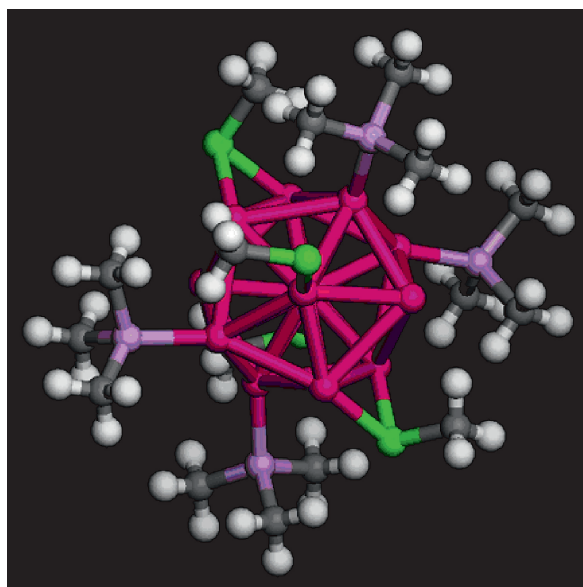
Nanoscale Atomic Clusters, Complexity of, Figure 7

Core atom counts for gold clusters measured using the quantitative HAADF-STEM technique for the mixed ligand (a) and thiolate-protected clusters (b), respectively, plotted against measured particle diameters. The blue, red and black lines are the spherical, hemispherical and monolayer island (111) models. The black and green dots are the data and the sample average. Reprinted with permission from [100]

lates may have distinctly different bonding motifs: on-top for phosphines [103] and bridge sites for thiolates [104]. Thus, the preferred ligand placement remains ambiguous. Second, the experimental distribution of Au-Au bond lengths was $\sigma^2 = 0.017 \pm 0.005 \text{ \AA}^2$, which is much larger than in bulk gold (0.008 \AA^2) at the same temperature (300 K) [59]. Such enhanced σ^2 must be configurational in nature, because the temperature-dependent, dynamic component in nanoparticles has previously exhibited only weak, if any, size dependence [68]. However, neither EXAFS nor TEM provides enough information to uncover its origin.

Guliamov et al. [105] used the EXAFS and TEM results as a starting point for a theoretical analysis based on density functional theory (DFT) [106] of the mixed-ligand Au_{13} nanocluster, $\text{Au}_{13}[\text{PPh}_3]_4[\text{S}(\text{CH}_2)_{11}\text{CH}_3]_4$. For bare Au_{13} nanoclusters, many structures—including icosahedral [107], cuboctahedral [108], biplanar [109], and amorphous [110] ones—have been predicted theoretically as comprising the lowest energy configuration. Both ordered and disordered structures were predicted theoretically for ligated Au_{38} structures [111,112,113] and experimental verification was limited to scattering methods (e.g., x-ray diffraction) which are less than ideal for clusters of this size. This may reflect the existence of several energetically close isomers [113].

Calculations of different ligand structures relaxed from an initial icosahedral Au core geometry established that the symmetric bonded-ligand configuration, shown in Fig. 8, is energetically preferable. Here, the results of the calculations were found to be in good *quantitative* agreement with the EXAFS data: The mixed on-top and bridge thiol geometry was maintained, the average Au-Au bond length was 2.88 \AA with a standard deviation of $\sigma^2 = 0.018 \text{ \AA}^2$, the coordination number, $N_{\text{Au-L}}$, was 0.77, and



Nanoscale Atomic Clusters, Complexity of, Figure 8

Optimized structure of the icosahedral Au_{13} cluster. Red: Au; Green: S; Purple: P; Gray: C; White: H

the average Au-ligand distance was 2.35 \AA , i.e., in good agreement with all experimental results [59].

Further analysis of the ligand-induced deviation from the ideal icosahedral symmetry of the Au core reveals that the variation in the radial distances from the central atom to the other Au atoms is very small: $R(\text{Au-Au})_{\text{rad}} = 2.78 \text{ \AA}$ with $\sigma^2 = 0.005 \text{ \AA}^2$. However, the in-shell tangential Au-Au bond lengths exhibit a much greater dispersion: $R(\text{Au-Au})_{\text{tan}} = 2.92 \text{ \AA}$ with $\sigma^2 = 0.017 \text{ \AA}^2$, with the smallest distance found between two thiol-ligated Au atoms and the largest between one thiol-ligated and one free Au atom. This is consistent with the

strong covalent interaction expected between the S and Au atoms [114,115]. For comparison, we studied the radial versus tangential bond length distribution in the relaxed, bare icosahedral Au_{13} . There, we found $R(\text{Au-Au})_{\text{rad}} = 2.73 \text{ \AA}$ and $R(\text{Au-Au})_{\text{tan}} = 2.87 \text{ \AA}$.

The above results clearly reveal that the tangential strain induced by the ligands is much larger than the radial one. Both radial and tangential bond lengths in the ligated cluster are larger by $\sim 1.8\%$ with respect to the bare one, but the induced dispersion in tangential bond lengths is much larger than in the radial ones. These findings can be interpreted via a combination of the asymmetry of the effective pair potential and the non-close-packed structure of the icosahedron. The ligands do not disorder the relatively stiff radial bonds, but do disorder atoms within the shell. The results suggest that it is the weakness of the in-shell Au-Au bonds, and thus lower energy penalty compared to the strong radial Au-Au bonds, that relieves otherwise strong stresses due to the asymmetry in the nature and bonding sites of thiolate and phosphine ligands.

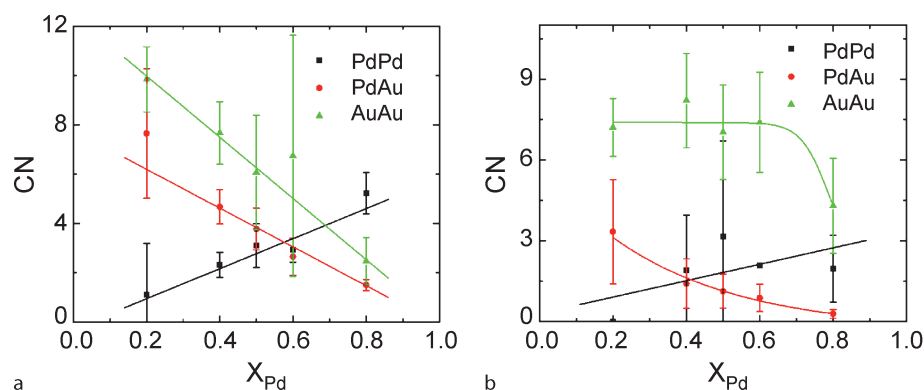
Experimental characterization of randomness of atomic distribution may be found by EXAFS. It is done by comparing experimental values of metal-metal coordination numbers against the model of (Fig. 3). For example, dendrimer-stabilized Pd/Au nanoalloys [116] are shown to be quasi-random or core-shell like, depending on the details of their preparation (Fig. 9).

This method is a powerful tool for quantifying short-range order in monodisperse clusters. However, a broad range of composition is required, to make such determination. If only one composition is available, the answer may be obtained from the combination of EXAFS, advanced electron microscopies (EDS, HREM, STEM) and DFT calculations. For example, EDS method revealed that the distribution of Pt:Ru was uniform, where each nanocluster

contained both Pt and Ru. Using the Z-contrast method for determining the number of atoms, Yang et al. [117] discovered that the average measured scattering cross-section corresponded to four PtRu_5 groups or 24 atoms. The diameters of these clusters were also measured from the STEM (Fig. 10) as well as by HREM, and the average was 15.6 \AA . Using an averaged number density of Ru and Pt, if the shape of the cluster is spherical, then, for a diameter of 15 \AA , the particle contains 21 PtRu_5 groups, whereas for a hemispherical shape, the cluster contains 11 PtRu_5 groups. These data shows that the particles are “raft-like” on the carbon black.

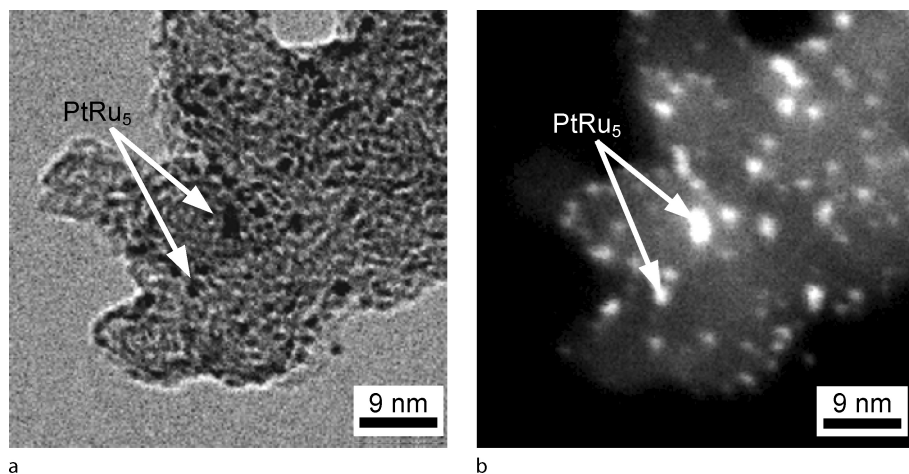
To demonstrate this point, Fig. 11 is a plot of the cluster diameter vs. the number of atoms per cluster for different 3-dimensional shapes. The two theoretical fits show the number of atoms for a (a) spherical shape with diameter, d , and (b) a hemispherical shape. Clearly, since the number of atoms is considerably less than would be predicted for a hemisphere, this demonstrates that the structure of the PtRu_5 is oblate on the carbon black support [117]. This result confirms the *truncated* cuboctahedral model proposed by Nashner et al. [94] based on results of their EXAFS analysis.

Wang et al. [118] confirmed EXAFS and electron microscopy results using DFT calculations, including the experimentally observed enhanced Pt-Pt bond length disorder. They revealed the origin of this disorder as due to the cluster/carbon-support interactions when samples are annealed in helium, whereas samples treated in hydrogen have disorder controlled by intraparticle effects, as discussed later. They explained the EXAFS observations that supported $[\text{PtRu}_5]$ metal clusters have fcc (111) cuboctahedral geometry and bulk-like metal-metal bond distances, even for small nanoparticles for which the average coordination number is much smaller than that in the



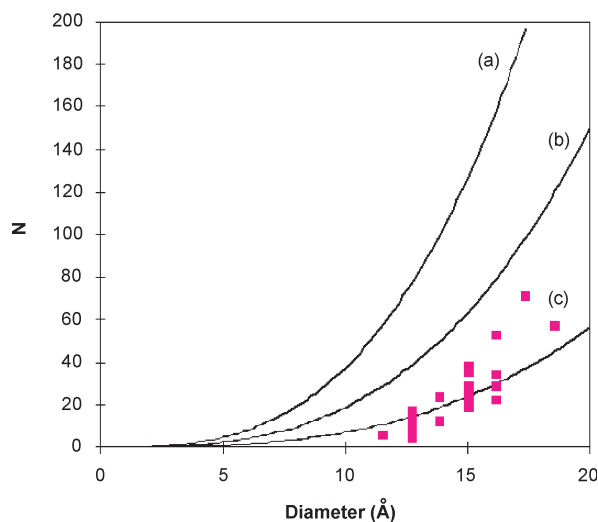
Nanoscale Atomic Clusters, Complexity of, Figure 9

Coordination numbers in nanoalloys: quasi-random dendrimer-stabilized Pd/Au alloys (a), and core-shell alloys (b). Samples courtesy of Crooks RM, U. of Texas at Austin



Nanoscale Atomic Clusters, Complexity of, Figure 10

BF image of PtRu₅ (a) and the corresponding HAADF image (b). Reprinted from [117]



Nanoscale Atomic Clusters, Complexity of, Figure 11

Plot of diameter vs. number of atoms for different shapes: **a** Sphere, **b** Hemisphere and **c** are the experimental data with the best fit where the 3-D aspect ratio is kept constant. Reprinted from [117]

bulk, and that Pt in the bimetallic clusters segregates to the top (111)-layer of the nanoparticle, as hypothesized based on EXAFS results.

Structural Relaxation of Nanoparticles

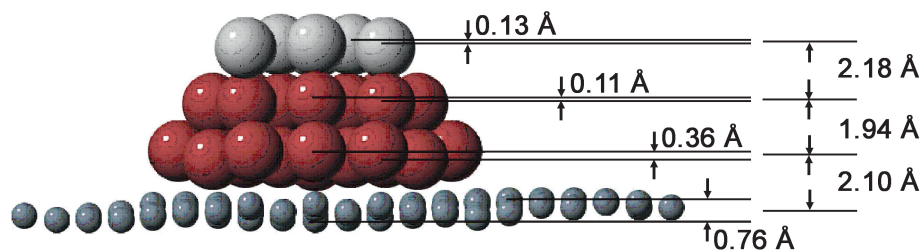
The data discussed above illustrate one level of new knowledge that comes from direct measurements of atomic scale structure. It is useful, though, to look at additional levels of insight that can be developed from data of this sort. Metal nanoclusters contain many distinct types of atoms – the

various habits found at the cluster surfaces, those residing at the metal support interface or cluster core, etc. [119] The metal-metal bonding, as a result of this diversity, is present as an ensemble embedding substantial configurational, static (as opposed to vibrational, dynamic) disorder.

Structural Relaxation in Freestanding and Supported Clusters

The case of the icosahedral Au clusters provides an interesting example in this regard. In this case, one moment of this effective disorder in the first shell bonding can be isolated and this in turn enables one to evaluate separately the nature of the icosahedral strain that it embeds. The latter parameter is one that directly illustrates the nature of the energetics that selects such non-bulk habits for the smallest clusters. The EXAFS analysis (Fig. 5a, inset) revealed the presence of an icosahedral strain of ca. 2.5% as compared to the 5% strain predicted by geometrically. This strain relaxation is correlated with and can be understood in terms of the ligand bonding – the simplest model of a support interaction (see below) – that terminate the cluster's surface. Obtaining such levels of structural understanding, however, is only possible if the synthetic protocols used deliver samples that are comprised of extremely monodispersed nanoparticles, a condition where it becomes possible to discriminate intra vs inter particle disorder (where the latter arises as a result of size-dependent atomic bond-length relaxation [61,85]).

It is also now well understood that more general forms of structural relaxations are common to the energy landscapes of supported metal clusters. The smallest clusters,

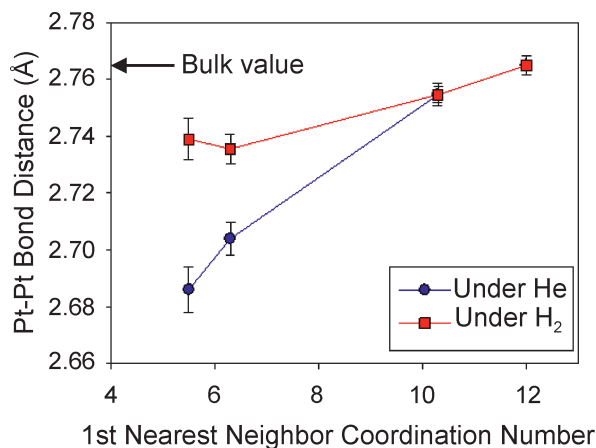


Nanoscale Atomic Clusters, Complexity of, Figure 12

Side view of the relaxed structures calculated with DFT-LDA for PtRu clusters supported on a graphite surface. The *small dark sphere* stands for C atoms, *large light (dark) spheres* for Pt (Ru) atoms. Both the intra-layer buckling and inter-layer distance are listed. Reprinted with permission from [118]

for example, are known to show contractions of their metal-metal bonding distances, [85] an outcome that can be understood intuitively in the context of the large number of non-bulk like atoms that would be found in a cluster that is 1nm in size – the relative fractions of surface and support-bonded atoms being large in such cases.

The data in Fig. 13 illustrate this point in greater detail, highlighting EXAFS measurements made on a series of rigorously characterized Pt catalysts supported on γ -Al₂O₃ [9]. As synthesized, the cluster distributions of atomic mass were held to exceptionally low values (a property stiffly characterized by microscopy). The data show the strong size dependent scaling of the average first-shell Pt-Pt bonding distances found in these samples. These distances are plotted here in terms of the number of first shell neighbors found experimentally by EXAFS, a parameter that explicitly correlates with both the particle's shape and diameter (as discussed for the data presented in Fig. 3, and for these samples showing by microscopy diameters

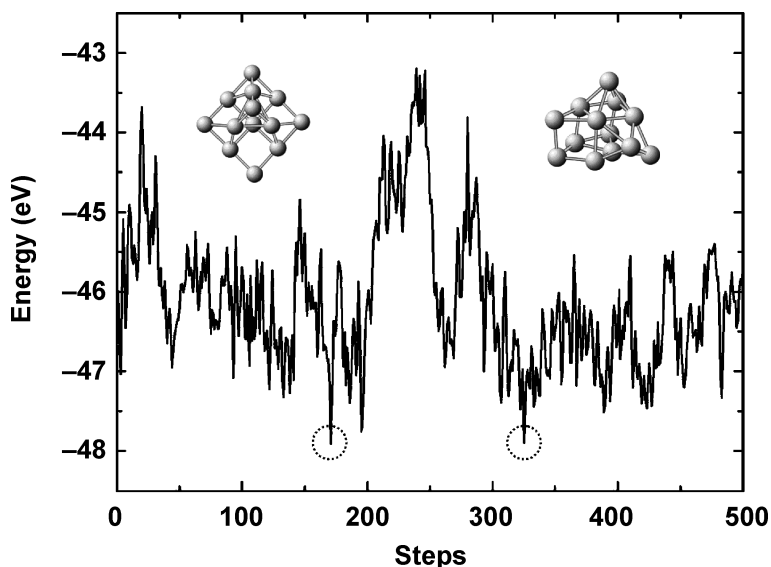


Nanoscale Atomic Clusters, Complexity of, Figure 13

The size-correlated average first shell M-M bonding distances for a series of Pt catalysts supported on γ -Al₂O₃

spanning a range from 0.9 to 2.8 nm). The sample with the smallest Pt particles (0.9 nm) consisted of a highly homogeneous sample of Pt₁₅ clusters (HAADF-STEM). The EXAFS data illustrate that size effects, in this case, elicit strong contractions of the metal-metal bonding distances – a structural relaxation that also develops a correlated and significant degree of interatomic disorder in the catalytic clusters. These relaxations are responsive to the presence of adsorbates – the data in the figure illustrate that hydrogen, which dissociates and passivates the surface bonds of the clusters lifts the relaxations (albeit not fully to bulk values for all but the largest clusters). The larger body of data implicitly suggests a model for the structural relaxations in which the bonding present at the ambient cluster surfaces/interfaces play an exceptionally important role – establishing the biases seen in the average distances and effective disorder measured by EXAFS.

Advances made in the first principle theory and MD simulations allow one to investigation of structural relaxation and relative stability of various cluster morphologies. Nonetheless, DFT-based simulations must be carefully validated before use in each system. For example, Wang and Johnson [120] have shown that *N*-atom (for $N \leq 20$) cluster morphologies are highly sensitive to the DFT exchange-correlation functional, and standard generalized gradient corrected, local (spin) density approximation often yield incorrect structural properties and energetics compared to high-level quantum chemistry. In addition, with the numerous geometrical and chemical configurations associated with finding ground state and lowest-energy excited-state morphologies (e. g., as in Fig. 1), one cannot be assured with absolute certainty that a simulation has found the absolute ground state for comparison to observation because the simulation times are short (order of nanoseconds to pico-seconds) and starting geometries are few. In this regard, the most commonly employed global-optimization strategies are simulated annealing (sometimes combined, e. g., see [4] with empirical



Nanoscale Atomic Clusters, Complexity of, Figure 14

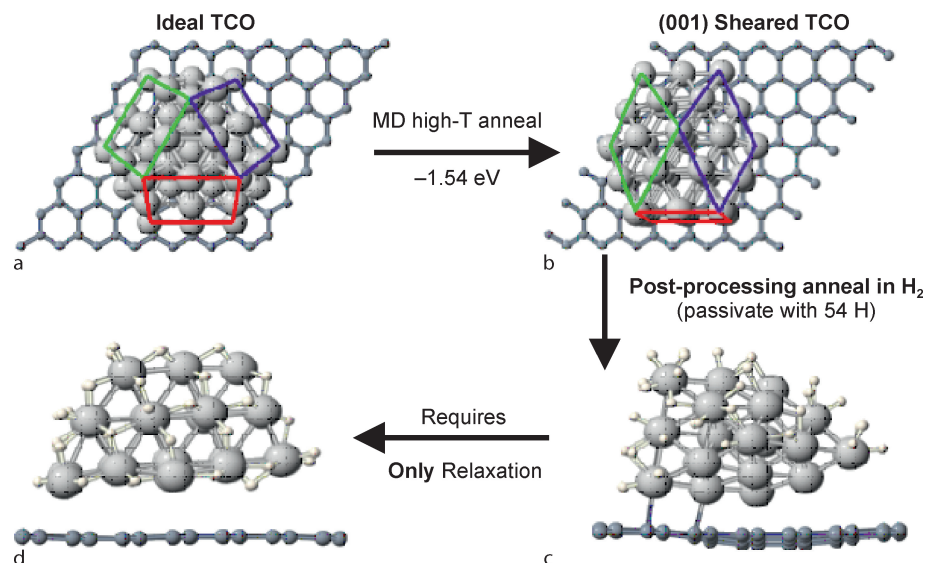
First-principles MD global (potential energy surface) optimization for 500 time steps for a Pt_{13} cluster that starts with an O_h cluster. Simulation was held at 2000 K for 4 to 10 picoseconds at time steps of 20 femtoseconds and used a single k -point in a periodic box with large vacuum. Two low-energy basins are circled, with their corresponding structures shown in insets after full relaxation of the cluster. All structures in Fig. 1 were found using this approach. Reprinted figure with permission from [3]

force-fields not containing proper cluster correlation effects), genetic and evolutionary algorithms (e. g., see example review [121] and with improved GAs [122]), and variants of basin-hopping that utilize temperature as a tunable parameter to sample large, but not all, portions of solution space (e. g., Monte Carlo [123] and molecular dynamics [3,4] using very small (not converged) k -meshes). Genetic algorithms and basin hopping are comparable in efficiency, both superior to simulated annealing. An example of basin hopping within MD is shown in Fig. 14, and used to obtain results in Fig. 1.

An illustrative example of DFT studies of structural relaxation and morphological transitions in nanoparticles is shown in Fig. 15, where Wang et al. [118] were able to characterize fully the adsorbate-dependent morphological habits of a model Pt_{37} cluster supported on carbon. Importantly, for comparison to experiment, consideration was made for the annealing stages in the synthesis, including post-processing in hydrogen atmosphere before characterization. With an anneal in hydrogen, the preferred structural habit for the cluster is a truncated cuboctahedron with large Pt-Pt bond length disorder in the bond distribution (from 2.62 to 2.93 Å) that arises from structural anisotropy within a cluster. This disorder is highest for bare clusters and is reduced when hydrogen atoms are allowed to adsorb. The disorder seen in each case provides a near quantitative agreement with values deduced from experiment [118,124]. These DFT calculations further re-

veal that the Pt_{37} truncated cuboctahedron (TCO, shown in Fig. 15a) has a morphological instability driven by the shearing of (100) to (111) facets to lower the surface energy (see Fig. 15b) – a remnant of the electronic mechanism responsible for (100)-surface reconstruction in semi-infinite bulk Pt. [124] However, with H passivation, this shear instability is removed and the TCO is highly stable, [124] as observed in experiments [94] and which is clearly a result of the annealing in H_2 .

Theory also predicts that M-M bond length contractions occur – ones that vary substantially with the presence of adsorbate bonding. They found, for example, that the DFT derived average first nearest neighbor Pt-Pt bond length for the model Pt_{37} cluster increases by 3% with H passivation (2.68 Å without H to 2.75 Å with H) [124]. These values provide a remarkable agreement with those determined experimentally (EXAFS 2.75 Å) when samples are annealed in hydrogen [68] versus helium [9]. Importantly, H-passivation effect on the Pt-Pt bond lengths are strongly dependent on the size of the cluster (both in simulations and observed); for smaller Pt nanoparticles with 1st shell coordination number (CN) from 5 to 7, an increase in Pt-Pt bond lengths is observed on various supports, whereas, for larger clusters with CN beyond 8 (i. e., approaching bulk CN of 12), no such effect is observed. The reason being that the relation between 1st shell CN and particle size is not linear, but roughly proportional to the \sqrt{D} , the particle diameter ($D = 2R$).



Nanoscale Atomic Clusters, Complexity of, Figure 15

Synopsis of the calculated DFT morphological changes of the structure of a Pt_{37} cluster on a carbon support during high-temperature anneal and post-processing anneal in H_2 performed during synthesis of real samples, see [124] for details. **a** High-T anneal of the ideal cuboctahedral (TCO) cluster, which **b** lowers its energy by internal shear of all (100) facets (shown by the red, green and blue planes) such that they resemble (111) facets, a mechanism which is a remnant of the electronically-driven shear instability for surface reconstruction in semi-infinite bulk Pt. For direct comparison to experiment, **c** the structure found in simulated post-processing anneal in H_2 , which **d** structurally reverts simple by relaxation (downhill in energy) to the observed cuboctahedral structure, showing then negligible interaction with the carbon support. For structural comparison to experiment, see text. Reprinted with permission from [118]

Clearly, careful implementation and validation of theory not only shows excellent agreement with a range physical properties (from bond-length distributions, structural parameters, electronic properties, etc.) but also reveals the key physics controlling these manifested behaviors, including the important of cluster-support interactions and charge transfer that impacts the structural and concomitant catalytic behavior, so highly prized for technological purposes.

Future Directions

With respect to the atomic arrangements present in nanoparticles, the availability of a new state of the art instruments for studies by electron microscopy and x-ray absorption spectroscopy provides an exceptional opportunity to gain new levels of understandings of the structural motives present in these systems. We believe that direct imaging of the 3D atomic arrangement present in such clusters will become eventually possible. When the future synchrotron sources with exceptional brightness (equivalent to the counting statistics of 10^{12} photons/sec at the 1nm focal spot) become available, it will become possible to measure structural dynamics in individual nanopar-

ticles by EXAFS. With the newest electron microscopes (e.g., JEOL (JEM) 2200F), high-resolution electron microscopy imaging will be possible with dramatically better resolution and, hence, improved interpretability. Since the spherical aberration causes delocalization in the images proportional to Θ^3 , where Θ is the Bragg angle of the diffracted beam, the reduction of the spherical aberration will eliminate the presence of “ghost” images and/or fringes, leading to significantly improved clarity of images. The focal series reconstruction of exit wavefunction can further improve the HREM interpretability. Because of the ability to obtain spectral information atomic-by-atomic column, changes in the EELS signal across a single nanoparticle, from the surface to the interface, will be achievable. This will provide detailed information about individual arrangement of atoms within an individual particle, such as core-shell structure or surface segregation. Furthermore, with the significantly improved HAADF-STEM imaging resolution to 1Å, significantly better than the 1nm³ tomography resolution available on modern non-aberration corrected instruments [125]. Additional possibilities that are being engendered by methods of coherent electron diffraction further suggest that it may be possible to vastly exceed the capabilities afforded by even

the very advanced capabilities of the JEOL 2200F instrument for electron tomography. For example, via over-sampling and phase retrieval it will be possible to invert a measured single cluster nano-diffraction pattern to obtain an atomic resolution 3D structure directly [126].

Current theoretical methods will be extended by enabling DFT-based calculations to identify low-energy structures, utilizing a rapid – optimization and selection protocols that appear to be well suited to applications involving supported nanoscale materials. An example is the DFT-based MD approach, in which the simulated nanocluster is heated to high temperature (e.g., 2000 K) and simulated rapidly using a coarse *k*-space mesh, is used to identify (relatively) rapidly several low-energy conformations, see Figs. 1 and 14. These conformations are then revisited with DFT-MD with a fine *k*-space mesh and configurations are then identified after full ionic relaxations. In the future, such protocols will be integrated with improved DFT exchange-correlation functionals to explore the nature of the energy landscapes that define the accessible and correct structures for a large variety of classes of nanoscale materials. Note that improved DFT exchange-correlation functionals [127,128,129,130,131,132,133,134,135] (such as hybrid B3LYP or PBE0, WC, and HSC) are computationally much more expensive than standard gradient corrected or local density approximation but yield much more correct results for nanoparticles, surface interactions, and some solid phases, such as ferroelectrics, which are highly sensitive to volume errors.

Complexity of nanoscale clusters can be quantitatively understood. However, due to the complexity of the characterization approaches that such understanding demands, only self-consistent, integrated, multi-disciplinary analysis methodologies appear to be heading in the direction of systematically solving their mysteries.

Acknowledgments

We are grateful to S. Sanchez, L. Li, A. Urban, L.-L. Wang, F. Dukesz and Q. Wang for help in preparing this manuscript. We would like to thank R.M. Crooks, M. Knecht and M. Meir for sharing samples used in these studies. We acknowledge support by the US Department of Energy (DOE) Grant No. DE-FG02-03ER15476.

Bibliography

Primary Literature

- Lai SL, Guo JY, Petrova V, Ramanath G, Allen LH (1997) Size-dependent melting properties of small tin particles: nanocalorimetric measurements. *Phys Rev Lett* 77:99–102
- Jesser WA, Shneck RZ, Gile WW (2004) Solid-liquid equilibria in nanoparticles of Pb-Bi alloys. *Phys Rev B* 69(14):144121
- Wang LL, Johnson DD (2007) Density functional study of structural trends for late-transition-metal 13-atom clusters. *Phys Rev B* 75:235405
- Futschek T, Marsman M, Hafner J (2005) Structural and magnetic isomers of small Pd and Rh clusters: an ab initio density functional study. *J Phys Condens Matter* 17:5927–5963
- Futschek T, Hafner J, Marsman M (2006) Stable structural and magnetic isomers of small transition-metal clusters from the Ni group: an ab initio density-functional study. *J Phys Condens Matter* 18:5703–5748
- Ferrando R, Jellinek J, Johnston RL (2008) Nanoalloys: From theory to applications of alloy clusters and nanoparticles. *Chem Rev* 108(3):845–910
- Baletto F, Ferrando R (2005) Structural properties of nanoclusters: Energetic, thermodynamic, and kinetic effects. *Rev Mod Phys* 77:371–423
- Daniel MC, Astrue D (2004) Gold nanoparticles: assembly, supramolecular chemistry, quantum-size-related properties, and applications toward biology, catalysis, and nanotechnology. *Chem Rev* 104(1):293–346
- Kang JH, Menard LD, Nuzzo RG, Frenkel AI (2006) Unusual non-bulk properties in nanoscale materials: thermal metal-metal bond contraction of γ -alumina-supported Pt catalysts. *J Am Chem Soc* 128:12068–12069
- Kamat PV (1993) Photochemistry on nonreactive and reactive (semiconductor) surfaces. *Chem Rev* 93:267–300
- Gates BC (1995) Supported metal clusters: synthesis, structure, and catalysis. *Chem Rev* 95:511–522
- Shahbazyan TV, Perakis IE (1999) Size-dependent correlation effects in the ultrafast optical dynamics of metal nanoparticles. *Phys Rev B* 60(12):9090–9099
- Tsunoyama H, Sakurai H, Tsukuda T (2006) Size effect on catalysis of gold clusters dispersed in water for aerobic oxidation of alcohol. *Chem Phys Lett* 429:528–532
- Roucoux A, Schultz J, Patin H (2002) Reduced transition metal colloids: A novel family of reusable catalysts. *Chem Rev* 102:3757–3778
- Schmid G (2006) Metal Nanoparticles, Synthesis of. In: *Encyclopedia of Inorganic Chemistry*, 2nd edn, vol 5. Wiley-VCH, Weinheim
- Taneja R, Chandra R, Banerjee R, Ayyub P (2001) Structure and properties of nanocrystalline Ag and Cu₂O synthesized by high pressure sputtering. *Script Mater* 44:1915–1918
- Spadavecchia J, Prete P, Lovergine N, Tapfer L, Rella R (2005) Au nanoparticles prepared by physical method on Si and sapphire substrates for biosensor applications. *J Phys Chem B* 109:17347–17349
- Mafune F, Jun-ya K, Takeda Y, Kondow T (2002) Full physical preparation of size-selected gold nanoparticles in solution: laser ablation and laser-induced size control. *J Phys Chem B* 106(31):7575–7577
- Ramachandra Rao CN, Kulkarni GU, Thomas PJ, Peter P Edwards (2000) Metal nanoparticles and their assemblies. *Chem Soc Rev* 29:27–35
- Giesen B, Orthner HR, Kowalik A, Roth P (2004) On the interaction of coagulation and coalescence during gas-phase synthesis of Fe-agglomerates. *Chem Eng Sci* 59:2201–2211

- Kamat PV, Flumiani M, Hartland GW (1998) Picosecond dynamics of silver nanoclusters. Photoejection of electrons and fragmentation. *J Phys Chem B* 102:3123–3128
- Kurita H, Takami A, Koda S (1998) Size reduction of gold particles in aqueous solution by pulsed laser irradiation. *Appl Phys Lett* 72:789–791
- Takami A, Kurita H, Koda S (1999) Laser-induced size reduction of noble metal particles. *J Phys Chem B* 103(8):1226–1232
- Hirai H, Nakao Y, Toshima N (1978) Colloidal rhodium in poly(vinylpyrrolidone) as hydrogenation catalyst for internal olefins. *Chem Lett* 7(5):545–548
- Kiwi J, Gratzel M (1979) Protection size factors, and reaction dynamics of colloidal redox catalysis mediating light induced hydrogen evolution from water. *J Am Chem Soc* 101:7214–7127
- Chechik V, Crooks RM (2000) Dendrimer-encapsulated Pd nanoparticles as fluorous phase-soluble catalysts. *J Am Chem Soc* 122(6):1243–1244
- Harriman A, Thomas JM, Millward GR (1987) Catalytic and structural properties of iridium-iridium dioxide colloids. *New J Chem* 11:757–762
- Zhu J, Shen Y, Xie A, Qiu L, Zhang Q, Zhang S (2007) Photoinduced synthesis of anisotropic gold nanoparticles in room-temperature ionic liquid. *J Phys Chem C* 111(21):7629–7633
- McGilvray KL, Decan MR, Wang D, Scaiano JC (2006) Facile photochemical synthesis of unprotected aqueous gold nanoparticles. *J Am Chem Soc* 128:15980–15981
- Yang S, Wang Y, Qingfeng W, Zhang R, Ding B (2007) Colloids *Surf A: Physicochem Eng Aspects* 301:174–183
- Mallick K, Witcomb MJ, Scurrill MS (2004) Polymer stabilized silver nanoparticles: A photochemical synthesis route. *J Mat Sci* 39(14):4459–4463
- Lee J, Ryu J, Choi W (2007) Synthesis of gold and platinum nanoparticles using visible light activated Fe(III)-complex. *Chem Lett* 36:176–177
- Pei L, Mori K, Adachi M (2004) Formation process of two-dimensional networked gold nanowires by citrate reduction of AuCl_4^- and the shape stabilization. *Langmuir* 20(18):7837–7843
- Suslick KS, Choe SB, Cichowlas AA, Grinstaff MW (1991) Sonochemical synthesis of amorphous iron. *Nature* 353:414–416
- Didenko YT, McNamara WB, Suslick KS (1999) Hot spot conditions during cavitation in water. *J Am Chem Soc* 121:5817–5818
- Su CH, Wu PL, Yeh CS (2003) Sonochemical synthesis of well-dispersed gold nanoparticles at iced temperature. *J Phys Chem B* 107:14240–14243
- Jiang LP, Wang AN, Zhano Y, Zhang JR, Zhu JJ (2004) A novel route for the preparation of monodisperse silver nanoparticles via a pulsed sonoelectrochemical technique. *Inorg Chem Comm* 7:506–509
- Dhas NA, Gedanken A (1998) Sonochemical preparation and properties of nanostructured palladium metallic clusters. *J Mater Chem* 8(2):445–450
- Kan C, Cai W, Li C, Zhang L, Hofmeister H (2003) Ultrasonic synthesis and optical properties of Au/Pd bimetallic nanoparticles in ethylene glycol. *J Phys D* 36:1609–1614
- Fujimoto T, Terauchi SY, Umehara H, Kojima I, Henderson W (2001) Sonochemical preparation of single-dispersion metal nanoparticles from metal salts. *Chem Mater* 13:1057–1060
- Huang S, Ma H, Zhang X, Yong F, Feng X, Pan W, Wang X, Wang Y, Chen S (2005) Electrochemical synthesis of gold nanocrystals and their 1D and 2D organization. *J Phys Chem B* 109(42):19823–19830
- Rodríguez-Sánchez L, Blanco MC, López-Quintela MA (2000) Electrochemical synthesis of silver nanoparticles. *J Phys Chem B* 104:9683–9688
- Starowicz M, Stypula B, Banas J (2006) Electrochemical synthesis of silver nanoparticles. *Electrochem Comm* 8(2):227–230
- Zhou M, Chen S, Ren H, Wu L, Zhano S (2005) Electrochemical formation of platinum nanoparticles by a novel rotating cathode method. *Physica E* 27(3):341–351
- Ueda M, Dietz H, Anders A, Kneppel H, Meixner A, Plieth W (2002) Double-pulse technique as an electrochemical tool for controlling the preparation of metallic nanoparticles. *Electrochem Acta* 48:377–386
- Plieth W, Dietz H, Anders A, Sandmann G, Meixner A, Weber M, Kneppel H (2005) Electrochemical preparation of silver and gold nanoparticles: Characterization by confocal and surface enhanced Raman microscopy. *Surf Sci* 597:119–126
- Toshima N, Yonezawa T, Kushihashi K (1993) Polymer-protected palladium-platinum bimetallic clusters: preparation, catalytic properties and structural considerations. *J Chem Soc* 89:2537–2543
- Toshima N, Harada M, Yamazaki Y, Asakura K (1992) Catalytic activity and structural analysis of polymer-protected gold-palladium bimetallic clusters prepared by the simultaneous reduction of hydrogen tetrachloroaurate and palladium dichloride. *J Phys Chem* 96:9927–9933
- Han S W, Kim Y, Kim K (1998) Dodecanethiol-derivatized Au/Ag bimetallic nanoparticles: TEM, UV/VIS, XPS, and FTIR analysis. *J Colloid Interface Sci* 208:272–278
- Link S, Wang ZL, El-Sayed MA (1999) Alloy formation of gold-silver nanoparticles and the dependence of the plasmon absorption on their composition. *J Phys Chem B* 103:3529–3533
- Sun S, Murray CB, Weller D, Folks L, Moser A (2000) Monodisperse FePt nanoparticles and ferromagnetic FePt nanocrystal superlattices. *Science* 287:1989–1992
- Bian B, Hirotsu Y, Sato K, Ohkubo T, Makino A (1999) Structures and magnetic properties of oriented Fe/Au and Fe/Pt nanoparticles on $\alpha\text{-Al}_2\text{O}_3$. *J Electron Microscop* 48:753–758
- Liu HB, Pal U, Medina A, Maldonado C, Ascencio JA (2005) Structural incoherency and structure reversal in bimetallic Au-Pd nanoclusters. *Phys Rev B* 71:075403
- Dadge JW, Islam M, Dharmadhikari AK, Mahamuni SR, Aiyer RC (2006) Hyper-Rayleigh scattering in electrochemically synthesized Ag-Au coupled clusters. *J Phys Condens Matter* 18:5405–5413
- Mandal M, Kundu S, Ghosh SK, Pal T (2004) Micelle-mediated UV-photoactivation route for the evolution of $\text{Pd}_{\text{core}}\text{-Au}_{\text{shell}}$ and $\text{Pd}_{\text{core}}\text{-Ag}_{\text{shell}}$ bimetallics from photogenerated Pd nanoparticles. *J Photochem Photobiol A* 167:17–22
- Hirakawa K, Toshima N (2003) Ag/Rh bimetallic nanoparticles formed by self-assembly from Ag and Rh monometallic nanoparticles in solution. *Chem Lett* 32(1):78–79
- Kanamaru M, Shiraishi Y, Koga Y, Toshima N (2005) Calorimetric study on self-assembling of two kinds of monometallic nanoparticles in solution. *J Therm Analysis Calorim* 81:523–527

58. Wang Y, Toshima N (1997) Preparation of Pd-Pt bimetallic colloids with controllable core/shell structures. *J Phys Chem B* 101:5301–5303
59. Menard LD, Xu H, Gao S, Twisten RD, Harper AS, Song Y, Wang G, Douglas AD, Yang JC, Frenkel AI, Murray RW, Nuzzo RG (2006) Metal core bonding motifs of monodisperse icosahedral Au₁₃ and larger Au monolayer-protected clusters as revealed by x-ray absorption spectroscopy and transmission electron microscopy. *J Phys Chem B* 110(30):14564–14573
60. Wang X, Hanson JC, Frenkel AI, Kim JJ, Rodriguez JA (2004) Time-resolved studies for the mechanism of reduction of copper oxides with carbon monoxide: Complex behavior of lattice oxygen and the formation of suboxides. *J Phys Chem B* 108:13667
61. Frenkel AI, Nemzer S, Pister I, Soussan L, Harris T, Sun Y, Rafailovich MH (2005) Size-controlled synthesis and characterization of thiol-stabilized gold nanoparticles. *J Chem Phys* 123:184701–6
62. Sun Y, Frenkel AI, Isseroff R, Shonbrun C, Forman M, Shin K, Koga T, White H, Zhang L, Zhu Y, Rafailovich MH, Sokolov JC (2006) Characterization of palladium nanoparticles by using x-ray reflectivity, EXAFS, and electron microscopy. *Langmuir* 22(2):807–816
63. Frenkel AI, Frankel SC, Liu T (2005) Structural stability of giant polyoxomolybdate molecules as probed by EXAFS. *Phys Scripta T115*:721–723
64. Frenkel AI, Menard LD, Northrup P, Rodriguez JA, Zypman F, Glasner D, Gao SP, Xu H, Yang JC, Nuzzo RG (2007) Geometry and charge state of mixed-ligand Au₁₃ nanoclusters. *AIP Conf Proc* 882:749–751
65. See, e. g., Bonačić-Koutecký V, Fantucci P, Koutecký V (1991) Quantum chemistry of small clusters of elements of groups Ia, Ib, and IIa: fundamental concepts, predictions, and interpretation of experiments. *Chem Rev* 91(5):1035–1108
66. Pyykkö R (2004) Theoretical chemistry of gold. *Angew Chem Int Ed* 43:4412–4456
67. Gurman SJ (1995) Interpretation of EXAFS data. *J Synchrotron Rad* 2:56–63
68. Frenkel A, Hills C, Nuzzo R (2001) A view from the inside: Complexity in the atomic scale ordering of supported metal nanoparticles. *J Phys Chem B* 105(51):12689–12703 (Feature Article)
69. Zabinsky SI, Rehr JJ, Ankudinov A, Albers RC, Eller MJ (1995) Multiple-scattering calculations of x-ray-absorption spectra. *Phys Rev B* 52:2995–3009
70. Newville M (2001) IFEFFIT: interactive XAFS analysis and FEFF fitting. *J Synchrotron Rad* 8:322–324
71. Montejano-Carrizale JM, Aguilera-Granja F, Moran-Lopez JL (1997) Direct enumeration of the geometrical characteristics of clusters. *NanoStruct Mater* 8(3):269–287
72. Calvin S, Miller MM, Goswami R, Cheng SF, Mulvaney SP, Whitman LJ, Harris VG (2003) Determination of crystallite size in a magnetic nanocomposite using extended x-ray absorption fine structure. *J Appl Phys* 94(1):778–783
73. Lytle FW, Via GH, Sinfelt JH (1977) New application of extended x-ray absorption fine structure (EXAFS) as a surface probe-nature of oxygen interaction with a ruthenium catalyst. *J Chem Phys* 67:3831–3832
74. Sinfelt JH, Via GH, Lytle FW (1977) Extended x-ray absorption fine structure (EXAFS) of supported platinum catalysts. *J Chem Phys* 68:2009–2010
75. Via GH, Sinfelt JH, Lytle FW (1979) Extended x-ray absorption fine structure (EXAFS) of dispersed metal catalysts. *J Chem Phys* 71:690–699
76. Sinfelt JH, Via GH, Lytle FW (1980) Structure of bimetallic clusters. Extended x-ray absorption fine structure (EXAFS) studies of Ru–Cu clusters. *J Chem Phys* 72:4832–4844
77. Sinfelt JH, Via GH, Lytle FW, Greeger RB (1981) Structure of bimetallic clusters. Extended x-ray absorption fine structure (EXAFS) studies of Os–Cu clusters. *J Chem Phys* 75:5527–5537
78. Sinfelt JH, Via GH, Lytle FW (1982) Structure of bimetallic clusters. Extended x-ray absorption fine structure (EXAFS) studies of Pt–Ir clusters. *J Chem Phys* 76:2779–2789
79. Marques EC, Sandstrom DR, Lytle FW, Greeger RB (1982) Determination of thermal amplitude of surface atoms in a supported Pt catalyst by EXAFS spectroscopy. *J Chem Phys* 77(2):1027–1034
80. Meitzner G, Via GH, Lytle FW, Sinfelt JH (1983) Structure of bimetallic clusters. Extended x-ray absorption fine structure (EXAFS) studies of Rh–Cu clusters. *J Chem Phys* 78(2):882–889
81. Meitzner G, Via GH, Lytle FW, Sinfelt JH (1983) Structure of bimetallic clusters. Extended x-ray absorption fine structure (EXAFS) studies of Ir–Rh clusters. *J Chem Phys* 78(5):2533–2541
82. Meitzner G, Via GH, Lytle FW, Sinfelt JH (1983) Structure of bimetallic clusters. Extended x-ray absorption fine structure (EXAFS) studies of Re–Cu, Ir–Cu, and Pt–Cu clusters. *J Chem Phys* 83(1):353–360
83. Meitzner G, Via GH, Lytle FW, Sinfelt JH (1983) Structure of bimetallic clusters. Extended x-ray absorption fine structure (EXAFS) studies of Ag–Cu and Au–Cu clusters. *J Chem Phys* 83(9):4793–4799
84. Meitzner G, Via GH, Lytle FW, Sinfelt JH (1983) Structure of bimetallic clusters. Extended x-ray absorption fine structure (EXAFS) of Pt–Re and Pd–Re clusters. *J Chem Phys* 87(11):6354–6363
85. Mays CW, Vermaak JS, Kuhlmann-Wilsdorf D (1968) On surface stress and surface tension: II. Determination of the surface stress of gold. *Surf Sci* 12(2):134–140
86. Montano PA, Schulze W, Tesche B, Shenoy GK, Morrison TI (1984) Extended x-ray-absorption fine-structure study of Ag particles isolated in solid argon. *Phys Rev B* 30(2):672–677
87. Montano PA, Purdum H, Schenoy GK, Morrison TI, Schulze W (1985) X-ray absorption fine structure study of small metal clusters isolated in rare-gas solids. *Surf Sci* 156:228–233
88. Montano PA, Shenoy GK, Alp EE, Schulze W, Urban J (1986) Structure of copper microclusters isolated in solid argon. *Phys Rev Lett* 56(19):2076–2079
89. Jiang P, Jona F, Marcus PM (1987) Surface effects in metal microclusters. *Phys Rev B* 36(12):6336–6338
90. Finnis MW, Heine V (1974) Theory of lattice contraction at aluminium surfaces. *J Phys F* 4(4):L37–L41
91. Frenkel AI (1999) Solving the structure of nanoparticles by multiple-scattering EXAFS analysis. *J Synchrotron Rad* 6:293–295
92. Hwang BJ, Sarma LS, Chen JM, Chen CH, Shih SC, Wang GR, Liu DG, Le JF, Tang M (2005) Structural models and atomic distribution of bimetallic nanoparticles as investigated by x-ray absorption spectroscopy. *J Am Chem Soc* 127(31):11140–11145

93. Cowley JM (1965) Short-range order and long-range order parameters. *Phys Rev* 138(5A):A1384–A1389
94. Nashner MS, Frenkel AI, Adler DL, Shapley JR, Nuzzo RG (1997) Structural characterization of carbon-supported platinum-ruthenium nanoparticles from the molecular cluster precursor $\text{PtRu}_5\text{C}(\text{Co})_{16}$. *J Am Chem Soc* 119:7760–7771
95. Singhal A, Yang JC, Gibson JM (1997) STEM-based mass spectroscopy of supported Re clusters. *Ultramicroscopy* 67: 191–206
96. Thomas JM, Midgley PA (2004) High-resolution transmission electron microscopy. The ultimate nanoanalytical technique. *Chem Commun* 7:1253–1267
97. Ishizuka K (2004) FFT multislice method—the silver anniversary. *Microsc Microanal* 10(1):34–40
98. Liu J (2005) Scanning transmission electron microscopy and its application to the study of nanoparticles and nanoparticle systems. *J Electron Microsc* 54(3):251–278
99. Liu W (2007) Multi-scale catalyst design. *Chem Eng Sci* 62(13):3502–3512
100. Menard LD, Gao S, Xu H, Twisten RD, Harpe AS, Song Y, Wang G, Douglas AD, Yang JC, Frenkel AI, Nuzzo RG, Murray RW (2006) Sub-nanometer Au monolayer-protected clusters exhibiting molecule-like electronic behavior: Quantitative high-angle annular dark-field scanning transmission electron microscopy and electrochemical characterization of clusters with precise atomic stoichiometry. *J Phys Chem B* 110(26):12874–12883
101. Patterson AL (1939) The Scherrer formula for x-ray particle size determination. *Phys Rev* 56(10):978–982
102. Menard LD, Xu F, Nuzzo RG, Yang JC (2006) Preparation of TiO_2 -supported Au nanoparticle catalysts from a Au_{13} cluster precursor: Ligand removal using ozone exposure versus a rapid thermal treatment. *J Catal* 243(1):64–73
103. Bellon P, Manassero M, Sansoni MJ (1972) Crystal and molecular structure of tri-iodoheptakis(tri-*p*-fluorophenylphosphine)undecagold. *Dalton Trans* 1481–1487
104. Bellon PL, Cariati F, Manassero M, Naldini M, Sansoni M (1971) Novel gold clusters. Preparation, properties and x-ray structure determination of salts of octakis(triarylphosphine)enneagold. $[\text{Au}_9\text{L}_8]\text{X}_3$. *J Chem Soc Chem Commun* 1423–1424
105. Guliamov O, Frenkel AI, Menard LD, Nuzzo RG, Kronik L (2007) Tangential ligand-induced strain in icosahedral Au_{13} . *J Am Chem Soc Commun* 129:10978–10979
106. Hohenberg P, Kohn W (1964) Inhomogeneous electron gas. *Phys Rev* 136(3B):B864–B871; Kohn W, Sham L (1965) Self-consistent equations including exchange and correlation effects. *Phys Rev* 140(4A):A1133–A1138
107. Michaelian K, Rendón N, Garzón IL (1999) Structure and energetics of Ni, Ag, and Au nanoclusters. *Phys Rev B* 60(3): 2000–2010
108. Häberlen OD, Chung S, Stener M, Röscher N (1997) From clusters to bulk: A relativistic density functional investigation on a series of gold clusters Au_n , $n = 6, \dots, 147$. *J Chem Phys* 106(12):5189–5201
109. Chang CM, Chou MY (2004) Alternative low-symmetry structure for 13-atom metal clusters. *Phys Rev Lett* 93:133401–4
110. Darby S, Mortimer-Jones TV, Johnston RL, Roberts C (2002) Theoretical study of Cu–Au nanoalloy clusters using a genetic algorithm. *J Chem Phys* 116(4):1536–1550
111. Häkkinen H, Barnett RN, Landman U (1999) Electronic structure of passivated $\text{Au}_{38}(\text{SCH}_3)_{24}$ nanocrystal. *Phys Rev Lett* 82(16):3264–3267
112. Garzon IL, Rovira C, Michaelian K, Beltran MR, Ordejon P, Junquera J, Sanchez-Portal D, Artacho E, Soler JM (2000) Do thiols merely passivate gold nanoclusters? *Phys Rev Lett* 85(24):5250–5251
113. Häkkinen H, Walter M, Grönbeck H (2006) Divide and protect: Capping gold nanoclusters with molecular gold-thiolate rings. *J Phys Chem B* 110(20):9927–9931
114. Dubbois LH, Nuzzo RG (1992) The synthesis, structure, and properties of model organic surfaces. *Annu Rev Phys Chem* 43:437–463
115. Garzón IL, Beltrán MR, González G, Gutiérrez-González I, Michaelian K, Reyes-Nava JA, Rodríguez-Hernández JI (2003) Chirality, defects, and disorder in gold clusters. *Eur Phys J D* 24:105–109
116. Knecht MR, Weir MG, Frenkel AI, Crooks RM (2008) Structural rearrangement of bimetallic alloy PdAu nanoparticles to yield core/shell configurations. *Chem Mater* 20:1019–1028
117. Yang JC, Bradley S, Gibson JM (2003) The oblate structure of PtRu_5 supported on carbon black. *Mater Charact* 51:101–107
118. Wang LL, Khare SV, Johnson DD, Rockett AA, Chirita V, Frenkel AI, Mack NH, Nuzzo RG (2006) Origin of bulk-like structure and bond distributions of Pt_{37} and $\text{Pt}_6\text{Ru}_{31}$ cluster on carbon: comparison of theory and experiment. *J Am Chem Soc* 128(1):131–142
119. Oudenhuijzen MK, Van Bokhoven JA, Miller JT, Ramaker DE, Koningsberger DC (2005) *J Am Chem Soc* 127(5):1530–1540 (and references therein)
120. Wang LL, Johnson DD (2005) Removing critical errors for DFT application to transition-metal nanoclusters: correct ground-state structures of Ru clusters. *J Phys Chem B Lett* 109(49):23113
121. Johnston RL (2003) Evolving better nanoparticles: Genetic algorithms for optimising cluster geometries. *Dalton Trans* 4193–4207
122. Kumara S, Johnson DD, Goldberg DE (2007) Scalability of a hybrid extended compact genetic algorithm for ground state optimization of clusters. *Mater Manuf Process* 22(5):570–576
123. Wales DJ, Doye JPK (1997) Global optimization by basin-hopping and the lowest energy structures of Lennard-Jones clusters containing up to 110 atoms. *J Phys Chem A* 101(28):5111–5116
124. Wang LL, Johnson DD (2007) Shear instabilities in metallic nanoparticles: Hydrogen-stabilized structure of Pt_{37} on carbon. *J Am Chem Soc* 129(12):3658–3664
125. Arslan I, Yates TJV, Browning ND, Midgley PA (2005) Embedded nanostructures revealed in three dimensions. *Science* 309(5744):2195–2198
126. Zuo JM, Vartanyants I, Gao M, Zhang R, Nagahara LA (2003) Atomic resolution imaging of a carbon nanotube from diffraction intensities. *Science* 300(5624):1419–1421
127. Perdew JP, Emzerhof M, Burke K (1996) Rationale for mixing exact exchange with density functional approximations. *J Chem Phys* 105(22):9982–9985
128. Adamo C, Barone V (1999) Toward reliable density functional methods without adjustable parameters: The PBE0 model. *J Chem Phys* 110(13):6158–6170
129. Becke AD (1993) A new mixing of Hartree–Fock and local density-functional theories. *J Chem Phys* 98(2):1372–1377

130. Becke AD (1993) Density-functional thermochemistry. III. The role of exact exchange. *J Chem Phys* 98(7):5648–5652
131. Bylander DM, Kleinman L (1990) Good semiconductor band gaps with a modified local-density approximation. *Phys Rev B* 41(11):7868–7871
132. Becke AD (1996) Density-functional thermochemistry, vol IV. A new dynamical correlation functional and implications for exact-exchange mixing. *J Chem Phys* 104(3):1040–1046
133. Heyd J, Scuseria GE, Ernzerhof M (2003) Hybrid functionals based on a screened Coulomb potential. *J Chem Phys* 118(18):8207–8215
134. Heyd J, Scuseria GE (2004) Assessment and validation of a screened Coulomb hybrid density functional. *J Chem Phys* 120(16):7274–7280
135. Wu Z, Cohen RE (2006) More accurate generalized gradient approximation for solids. *Phys Rev B* 73(23):235116–235121

Books and Reviews

- Edelstein AS, Cammarata RC (eds) (1998) *Nanomaterials: Synthesis, Properties and Applications*. Institute of Physics Publishing, Bristol
- Heiz U, Landman U (eds) (2006) *Nanocatalysis*. Springer, Heidelberg

Nanoscale Processes, Modeling Coupled and Transport Phenomena in Nanotechnology

RODERICK MELNIK^{1,2}

¹ M²NeT Lab, Department of Mathematics, Wilfrid Laurier University, Waterloo, Canada

² Department of Physics, University of Waterloo, Waterloo, Canada

Article Outline

Glossary
 Definition of the Subject
 Introduction
 Hierarchy of Mathematical Models for LDSNs
 Numerical Methodologies
 Incorporating New Effects
 Applications and Concluding Remarks
 Acknowledgments
 Bibliography

Glossary

Low dimensional semiconductor nanostructures

Structures that have characteristic dimensions on the order of nanometers (usually between 1 and 100 nm) and such that the motion of electrons in them can be confined spatially. Quantum well heterostruc-

tures were the first low dimensional semiconductor nanostructures experimentally developed in the early 1970s. Now, a number of different techniques exist to produce a variety of different low dimensional semiconductor nanostructures, including quantum wells, wires, and dots.

Electronic structure Electrons move from one energy level to another by emission or absorption of a quantum of energy, a photon. They are placed on electronic orbitals and their configuration defines the electronic structure as the arrangement of electrons in an atom, molecule, etc. The knowledge of the electronic structure of a specific material or a structure helps us in predicting its properties.

Electromechanical effects One of the most studied examples of such effects is piezoelectricity, demonstrated for the first time by the brothers Pierre Curie and Jacques Curie in 1880. Now, it is one of the classical examples of coupled phenomena. In the heart of the piezoelectric phenomenon is a coupling mechanism between mechanical and electric fields which is a two-way interaction. In particular, electricity is produced in a piezoelectric body when stress is applied (the direct piezoeffect) and the body is stressed when an electric field is applied (the converse piezoeffect).

Multiple scales In studying complex systems we have to deal with coupled phenomena and processes at a multitude of different spatial and temporal scales. Understanding interactions in the system and its response at multiple scales is a fundamental quest of modern science.

Nanotechnology A multidisciplinary field that develops and extends our present knowledge into the nanoscale. It is the field where two main science and technology approaches, the “bottom-up” approach and the “top-down” approach, go hand in hand emphasizing the importance of systems science view.

Mathematical modeling A universal tool of modern science and technology that uses mathematical language to describe the behavior of systems, processes and phenomena in Nature and man-made.

Definition of the Subject

Low Dimensional Semiconductor Nanostructures (abbreviated, LDSNs) is a class of physical systems with characteristic dimensions on the order of 1–100 nm such that the motion of their charge carriers can be confined from one, two, or even three spatial dimensions. If we start our consideration from a three dimensional (3D) bulk crystal and create a structure where the motion of carriers is confined